

# Weather Prediction in SHiELD: Effect from GFDL Cloud Microphysics Scheme Upgrade

Linjiong Zhou<sup>1,2</sup>, Lucas Harris<sup>2</sup>, Jan-Huey Chen<sup>2,3</sup>, Kun Gao<sup>1,2</sup>, Huan Guo<sup>2</sup>,  
Baoqiang Xiang<sup>2,3</sup>, Mingjing Tong<sup>2</sup>, J. Jacob Huff<sup>2,3</sup>, and Matthew Morin<sup>2,3</sup>

<sup>1</sup>Program in Atmospheric and Oceanic Sciences, Princeton University, Princeton, New Jersey, USA.

<sup>2</sup>National Oceanic and Atmospheric Administration / Geophysical Fluid Dynamics Laboratory, Princeton,  
New Jersey, USA.

<sup>3</sup>University Corporation for Atmospheric Research, Boulder, Colorado, USA.

## Key Points:

- The GFDL cloud microphysics scheme has been re-written for greater physical consistency.
- The upgrade of the GFDL MP significantly improves weather prediction within the GFDL SHiELD model.
- The changes of PSD and CCNs in the GFDL MP show significant impacts on temperature, humidity, and cloud predictions.

---

Corresponding author: Linjiong Zhou, [Linjiong.Zhou@noaa.gov](mailto:Linjiong.Zhou@noaa.gov)

**Abstract**

This paper documents the third version of the GFDL cloud microphysics scheme (GFDL MP v3) used in the System for High-resolution prediction on Earth-to-Local Domains (SHIELD) model. Compared to the GFDL MP v2, the GFDL MP v3 is entirely reorganized, optimized, and modularized by functions. In addition, the particle size distribution (PSD) of all cloud categories is redefined to mimic the latest observations, and the cloud condensation nuclei (CCNs) are calculated from the MERRA2 aerosol data. The GFDL MP has been redesigned so all processes use the redefined PSD to ensure over-all consistency and easily permit introductions of new PSDs and microphysical processes.

Analyses gathered from simulations by SHIELD with selected configurations are examined. Compared to the GFDL MP v2, the GFDL MP v3 significantly improves the predictions of geopotential height, air temperature, and specific humidity in the Troposphere, as well as the high, middle and total cloud fractions and the liquid water path. With the more realistic PSD implemented in GFDL MP v3, the predictions of geopotential height in the Troposphere, low and total cloud fractions are further improved. Furthermore, using climatological aerosol data to calculate CCNs leads to even better predictions of geopotential height, air temperature, and specific humidity in the Troposphere, high and middle cloud fractions, as well as the liquid and ice water paths. However, the upgrade of the GFDL MP shows little impact on the precipitation prediction. Degradation due to the scheme upgrade is also addressed and discussed to guide the future GFDL MP development.

**Plain Language Summary**

The Geophysical Fluid Dynamics Laboratory (GFDL) cloud microphysics (MP) scheme has been recently upgraded to improve the code's structure and flexibility, and overall consistency, include more realistic cloud particle size distribution (PSD), and use the climatological aerosol to calculate cloud condensation nuclei (CCNs). The primary purpose of the GFDL MP upgrade is to improve global weather prediction, which includes geopotential height, temperature, specific humidity, cloud, and precipitation predictions. The implementation of the upgraded GFDL MP significantly improves the weather prediction of many key fields. Especially, the use of the more realistic cloud PSD and climatological aerosol for CCNs can further improve the prediction skill of the model to some extent.

**1 Introduction**

Clouds play critical roles in our daily weather and in the global energy and water budgets that regulate the climate of the Earth (Houze, 2014; Lamb & Verlinde, 2011). The formation and evolution of clouds have significant impacts on precipitation forecasts in numerical weather prediction (Baldauf et al., 2011; Bauer et al., 2015; Morrison & Grabowski, 2008; Seifert & Beheng, 2005). Clouds and their impacts on solar and thermal radiation are among the most challenging aspects of climate prediction (Stephens et al., 2012; Trenberth et al., 2009; Wild et al., 2019). Therefore, the representation of clouds in atmospheric models deserves particular attention. Since numerical models ranging from large-eddy simulations to climate predictions still cannot depict the cloud processes explicitly, the parameterization of cloud microphysics is needed (Kogan, 2013; Morrison & Gettelman, 2008; Nogherotto et al., 2016).

The national operational forecast system, Global Forecast System (GFS) at the National Centers for Environmental Prediction (NCEP), used the prognostic cloud microphysics scheme developed by Zhao and Carr (1997) from 1995 to 2019. Different from the simple large-scale saturation adjustment scheme (Hoke et al., 1989) used in the early versions of GFS, this prognostic cloud microphysics scheme explicitly calculates the com-

65 bined cloud water and cloud ice category in the large-scale condensation component of  
66 the model (Zhao et al., 1997). The cloud water/ice mass mixing ratio is the only vari-  
67 able predicted in the Zhao and Carr (1997) scheme for both cloud water and cloud ice.  
68 This treatment saves the model computational time and storage and has been used ex-  
69 clusively since 1995. According to Zhao et al. (1997), forecasts using the Zhao and Carr  
70 (1997) scheme improved the forecast skill of precipitation as measured by the equitable  
71 threat score and bias score and reduced root-mean-square errors of forecast specific hu-  
72 midity at all pressure levels below 800 hPa and above 500 hPa during test periods over  
73 those of forecasts that only used diagnostic clouds.

74 There is an apparent deficiency in the Zhao and Carr (1997) scheme. The oversim-  
75 plified treatment of cloud water and cloud ice inevitably excludes the interaction between  
76 cloud water and cloud ice, such as freezing and melting. As computational resources rapidly  
77 expand in recent decades, more sophisticated cloud microphysics schemes have been de-  
78 veloped and used in weather and climate models. For example, the European Centre for  
79 Medium-Range Weather Forecasts replaced the ancient Tiedtke (1993) scheme with the  
80 advanced Forbes and Tompkins (2011); Forbes et al. (2011) prognostic scheme for the  
81 Integrated Forecast System in 2010. The National Center for Atmospheric Research up-  
82 graded the Rasch and Kristjánsson (1998) prognostic condensate and precipitation scheme  
83 to the well-known Morrison and Gettelman (2008) scheme for the Community Atmosphere  
84 Model version 5 in 2012. Much research has shown that by using a more comprehensive  
85 cloud microphysics scheme, one can achieve better weather prediction and climate sim-  
86 ulation (Khain et al. (2015); Guo et al. (2021) and references therein). After extensive  
87 examinations with comprehensive verification, NCEP chose to replace the Zhao and Carr  
88 (1997) cloud microphysics scheme with the Geophysical Fluid Dynamics Laboratory (GFDL)  
89 cloud microphysics (MP) scheme (J. H. Chen & Lin, 2013; Zhou et al., 2019) in the GFS  
90 upgrade of June 2019, aiming to better represent the interaction between each cloud cat-  
91 egory to improve weather prediction.

92 The GFDL MP is a six-category, single-moment bulk microphysics scheme. Besides  
93 the water vapor category, there are two liquid categories (cloud water and rain) and three  
94 ice categories (cloud ice, snow, and graupel or hail). Zhou et al. (2019) and L. Harris,  
95 Zhou, Lin, et al. (2020) have described key features of the GFDL cloud microphysics scheme,  
96 including thermodynamic consistency with the dynamical core, fast and stable sedimen-  
97 tation processes, and tight coupling between dynamics and physics. The GFDL cloud  
98 microphysics scheme has been used as the default scheme in the operational GFS ver-  
99 sion 15 and 16 (Tong et al., 2020; Huang et al., 2021; Patel et al., 2021) and several other  
100 weather and climate models, including the GFDL radiative-convective equilibrium (RCE)  
101 simulations within a limited domain (Jeevanjee, 2017), the GFDL High-resolution At-  
102 mosphere Model (HiRAM) (J. H. Chen & Lin, 2011, 2013; L. M. Harris et al., 2016; Gao  
103 et al., 2017, 2019), the GFDL System for High-resolution prediction on Earth-to-Local  
104 Domains (SHiELD) (L. Harris, Zhou, Lin, et al., 2020), the National Oceanic and At-  
105 mospheric Administration’s Hurricane Analysis and Forecast System (HAFS) (Dong et  
106 al., 2020; A. Hazelton et al., 2021), the Chinese Academy of Sciences Flexible Global Ocean-  
107 Atmosphere-Land System Model (Zhou et al., 2015; Li et al., 2019; He et al., 2019), and  
108 the National Aeronautics and Space Administration Goddard Earth Observing System  
109 (GEOS) version 5 (Arnold et al., 2020).

110 Notably, the GFDL cloud microphysics scheme is now mainly developed within SHiELD  
111 at GFDL. Although the performance of SHiELD has gradually improved over the years  
112 with the continuous upgrades of the GFDL MP, cloud, precipitation, and radiation pre-  
113 dictions are still challenging. For example, ice cloud fraction is under-predicted and so  
114 the long-wave radiation at the top of the atmosphere is significantly over-estimated. Liq-  
115 uid cloud fraction is also largely under-predicted over the global ocean area. SHiELD  
116 tends to predict excessive light and extreme precipitation and under-predict medium pre-  
117 cipitation according to the analyses in L. Harris, Zhou, Lin, et al. (2020). The variable-

118 resolution SHiELD with the GFDL MP is still struggling in predicting the strength and  
119 location of the convective-scale precipitation over the contiguous United States (Zhou  
120 et al., 2019). Leighton et al. (2020) pointed out that an unrealistic representation of the  
121 particle size distribution of cloud condensates in cloud microphysics schemes leads to the  
122 limited representation of the cloud variability and degradation of tropical cyclone pre-  
123 diction. Fan et al. (2016) pointed out that aerosol-cloud interaction is essential and has  
124 significant impacts on radiative forcing, precipitation, extreme weather, and large-scale  
125 circulation in their review paper.

126 This paper aims to document the most recent upgrade of the GFDL cloud micro-  
127 physics scheme and understand the impacts of the more realistic particle size distribu-  
128 tion and the use of climatological aerosol for cloud condensation nuclei on the global tem-  
129 perature, humidity, cloud, and precipitation predictions, and serves as a reference for fu-  
130 ture development. This paper is organized as follows. Section 2 briefly introduces the  
131 model used in this study. Section 3 documents the upgrade of the GFDL cloud micro-  
132 physics scheme in detail. Section 4 presents the upgraded GFDL MP’s impacts on weather  
133 prediction via detailed verification. Section 5 demonstrates the effects of the realistic par-  
134 ticle size distribution and the use of climatological aerosol for cloud condensation nuclei  
135 on weather prediction. Finally, we end up with a summary and discussion in section 6.

## 136 2 Model Description

137 The model used in this study is the System for High-resolution prediction on Earth-  
138 to-Local Domains (SHiELD). SHiELD, previously called fvGFS (finite-volume Global  
139 Forecast System) (A. T. Hazelton et al., 2018; Zhou et al., 2019; J. Chen et al., 2019;  
140 J. H. Chen et al., 2019), was developed as a prototype of the Next-Generation Global  
141 Prediction System of the National Weather Service and the broader Unified Forecast Sys-  
142 tem (UFS) (L. Harris, Zhou, Lin, et al., 2020). SHiELD can be used for applications on  
143 a broad range of time scales but has been designed with a particular focus on weather  
144 (up to 10 days) (L. M. Harris et al., 2019) and subseasonal-to-seasonal (S2S; between  
145 two weeks and one season) (L. Harris, Zhou, Lin, et al., 2020) predictions. Notably, ad-  
146 vances in SHiELD have migrated into UFS models slated for operational implementa-  
147 tions at NCEP, including the GFS version 15 and version 16.

148 In this study, all SHiELD simulations use the non-hydrostatic solver within the Finite-  
149 Volume Cubed-Sphere Dynamical Core (FV3) developed at GFDL (L. M. Harris & Lin,  
150 2013; S.-J. Lin, 2004; Putman & Lin, 2007; L. Harris, Zhou, Chen, & Chen, 2020; L. Har-  
151 ris, Chen, et al., 2020). The physical parameterization suite in SHiELD originated from  
152 that in GFS version 14 (J. Chen et al., 2019), but contains substantial updates in the  
153 following processes: the microphysics scheme of Zhao and Carr (1997) and cloud frac-  
154 tion scheme of Xu and Randall (1996) are replaced by the inline GFDL cloud microphysics  
155 parameterizations (Zhou et al., 2019; L. Harris, Zhou, Lin, et al., 2020). The cloud-radiation  
156 interaction was redesigned to combine the cloud microphysics processes and cloud ra-  
157 diative properties. To incorporate atmosphere-ocean interaction, we have implemented  
158 a mixed layer ocean module based on Pollard et al. (1973). This simple ocean model com-  
159 puts the mixed layer depth and temperature within that mixed layer as prognostic vari-  
160 ables, driven by surface wind stress and heat fluxes from the atmosphere together with  
161 a nudging toward climatology applied to the mixed layer temperature and mixed-layer  
162 depth (L. Harris, Zhou, Lin, et al., 2020). In the latest version of SHiELD that is used  
163 in this paper, the convection schemes (J. G. Han et al., 2017), planetary boundary layer  
164 scheme (J. Han & Bretherton, 2019), and land surface model (Ek et al., 2003) are all up-  
165 dated to synchronize the current operational GFS version 16.

### 3 Cloud Microphysics Parameterization

The first version of the GFDL cloud microphysics scheme (GFDL MP v1, Zhou et al. (2019)) originated from J. H. Chen and Lin (2013), was mainly developed for fvGFS to support the upgrade of operational GFS version 15. It was a split cloud microphysics scheme in which the saturation adjustment processes were built inside the FV3 dynamical core. This version, with some minor upgrades, is still in use in the operational GFS version 16. Later the second version of the GFDL cloud microphysics scheme (GFDL MP v2, L. Harris, Zhou, Lin, et al. (2020)) was developed entirely inside the FV3 dynamical core in SHIELD. We call this the "inline GFDL MP". Recently, the GFDL MP in SHIELD has been dramatically updated. We call this the third version of the GFDL MP as it is significantly different from the second version. Compared with the GFDL MP v2, the code of the GFDL MP v3 is entirely reorganized, optimized, and modularized by functions for the first time. All scientific updates are described in Appendix A. The improvements from the GFDL MP v3 in weather prediction are demonstrated in the following sections.

Among all the updates in the GFDL MP v3, the update of particle size distribution and the overall consistency are essential and significant. First, the particle size distributions for all six cloud categories are redefined as a gamma distribution to mimic the latest observations. As a result, the cloud water and cloud ice are no longer mono-dispersed as in the GFDL MP v2. The large cloud categories, e.g., rain, snow, and graupel, or hail, still follow the exponential distribution as suggested by most observations and literature (Khain et al. (2015) and references therein), and which is a special case of the gamma distribution. Along with the particle size distribution upgrade, microphysical processes, e.g., accretion, evaporation, sublimation/deposition, and freezing/melting, have been reformatted and overhauled accordingly. This ensures an overall microphysical consistency and easily permits introductions of new particle size distributions, microphysical processes, and multi-moment distributions. Details of these updates are described in the following subsections. Due to the introduction of the more realistic particle size distribution and reformation of many microphysical processes, the computational runtime of the microphysics scheme increases by about 20%, but it is negligible (about 2%) compared to the total model runtime in SHIELD.

#### 3.1 Particle Size Distribution

The particle size distribution (PSD) describes the microstructure of a cloud category in each grid box. By definition, the concentration of a cloud particle is a function of the particle size. In general, the PSD functions can be mono-dispersed, exponential, gamma, or log-normal distribution. These distributions are normalizable and integratable over complete size distributions of diameter from zero to infinity, or partial distributions from diameter of zero to  $D_1$  or  $D_2$  to infinity or even  $D_1$  to  $D_2$  (Straka, 2009). All cloud properties and cloud processes can then be parameterized based on the PSD functions. In the GFDL MP v3, the PSD of each cloud category is parameterized with gamma distribution containing three parameters:

$$n(D) = n_0 D^{\mu-1} \exp(-\lambda D), \quad (1)$$

where  $n_0$  (unit:  $m^{-3-\mu}$ ) is called the intercept parameter,  $\mu$  (unit: 1) is called the spectral shape parameter,  $\lambda$  (unit:  $m^{-1}$ ) is called the slope parameter, and  $D$  (unit:  $m$ ) is the particle's diameter. When the spectral shape parameter  $\mu$  equals to 1, it becomes an exponential distribution. In a single-moment bulk cloud microphysics scheme with prognostic mass mixing ratio  $q$  (unit:  $kg\ kg^{-1}$ ), the intercept parameter  $n_0$  and spectral shape parameter  $\mu$  are predefined, while the slope parameter  $\lambda$  can be derived from  $n_0$ ,  $\mu$ , and  $q$ . The values of  $n_0$  and  $\mu$  for each cloud category of the GFDL MP v3 are listed in Table 1. Those parameters for cloud water, cloud ice, rain, snow, and graupel or hail are derived based on Martin et al. (1994), Fu (1996), Marshall and Palmer (1948),

**Table 1.** The intercept parameter ( $n_0$ , unit:  $m^{-3-\mu}$ ), spectral shape parameter ( $\mu$ , unit: 1), density of cloud category ( $\rho_0$ , unit:  $kg\ m^{-3}$ ), parameter  $\alpha$  (unit:  $m^{1-\beta}\ s^{-1}$ ) and  $\beta$  for each cloud category of the GFDL MP v3.

	Cloud Water	Cloud Ice	Rain	Snow	Graupel	Hail
$n_0$	$1.2 \times 10^{66}$	$1.0 \times 10^{10}$	$8 \times 10^6$	$3 \times 10^6$	$4 \times 10^6$	$4 \times 10^4$
$\mu$	11	1	1	1	1	1
$\rho_0$	$1 \times 10^3$	$9.17 \times 10^2$	$1 \times 10^3$	$1 \times 10^2$	$4 \times 10^2$	$9.17 \times 10^2$
$\alpha$	$3 \times 10^7$	11.72	842	4.8	1	1
$\beta$	2	0.41	0.8	0.25	0.5	0.5

217 Gunn and Marshall (1958), and Houze et al. (1979) or Federer and Waldvogel (1975),  
 218 respectively.

219 The particle size distribution (PSD) is not simply a function of diameter ( $D$ ), as  
 220 shown in Equation (1). It also depends on cloud content ( $\rho q$ ) or the mass mixing ratio  
 221 of cloud ( $q$ ) because the slope parameter ( $\lambda$ , defined below) is a function of  $q$ . Figure 1  
 222 shows that cloud water droplet number follows gamma distribution while all other cloud  
 223 categories follow exponential distribution at a specified cloud content. The particle num-  
 224 ber of cloud categories increases when cloud content increases. As shown in Figure 1a,b,  
 225 most cloud water droplets have sizes between  $6\ \mu m$  and  $40\ \mu m$ , with a peak particle num-  
 226 ber at around  $20\ \mu m$ . Cloud water droplet number is three orders of magnitude less when  
 227 the cloud water content drops from  $10\ g\ m^{-3}$  to  $10^{-4}\ g\ m^{-3}$ . Different from cloud wa-  
 228 ter, cloud ice particle number monotonically decreases as particle size increases (Figure  
 229 1c,d). As shown in Figure 1e-l, the distributions of rain, snow, graupel, and hail parti-  
 230 cle numbers are similar, except that rain has the highest particle number while hail has  
 231 the lowest particle number because rain (hail) has the highest (lowest) intercept param-  
 232 eter ( $n_0$ ). Rain, snow, graupel, and hail particle sizes approach zero at radii between  $2000$   
 233  $\mu m$  to  $6000\ \mu m$ , depending on the particular species and the water content. Higher wa-  
 234 ter content is needed to produce non-negligible numbers of the largest particles. In the  
 235 GFDL MP v3, cloud ice particle number still follows the exponential distribution as Fu  
 236 (1996). The same PSD assumption is applied to the calculation of cloud ice radiative prop-  
 237 erty. Recent studies, e.g., McFarquhar et al. (2015), used new observations to show cloud  
 238 ice should follow the gamma distribution. As the PSD of cloud ice is written in gamma  
 239 distribution format, we can change its PSD in the future.

### 240 3.2 Quantities Characterizing Cloud Parameters

241 Once the PSD is defined, we can derive the particle concentration ( $N$ , unit:  $m^{-3}$ ),  
 242 effective diameter ( $D_{\text{eff}}$ , unit:  $m$ ), optical extinction ( $\beta$ , unit:  $m^{-1}$ ), mass mixing ratio  
 243 ( $q$ , unit:  $kg\ kg^{-1}$ ), and radar reflectivity factor ( $Z$ , unit:  $m^3$ ) by integrating the PSD  
 244 over all diameters:

$$245 \quad N = \int_0^\infty n(D) dD = \frac{n_0 \Gamma(\mu)}{\lambda^\mu}, \quad (2)$$

$$246 \quad D_{\text{eff}} = \frac{\int_0^\infty D^3 n(D) dD}{\int_0^\infty D^2 n(D) dD} = \frac{\mu + 2}{\lambda}, \quad (3)$$

$$247 \quad \beta = \frac{\pi}{2} \int_0^\infty D^2 n(D) dD = \frac{\pi n_0 \Gamma(\mu + 2)}{2 \lambda^{\mu+2}}, \quad (4)$$

$$248 \quad q = \frac{\pi}{6} \frac{\rho_0}{\rho} \int_0^\infty D^3 n(D) dD = \frac{\pi \rho_0 n_0 \Gamma(\mu + 3)}{6 \rho \lambda^{\mu+3}}, \quad (5)$$

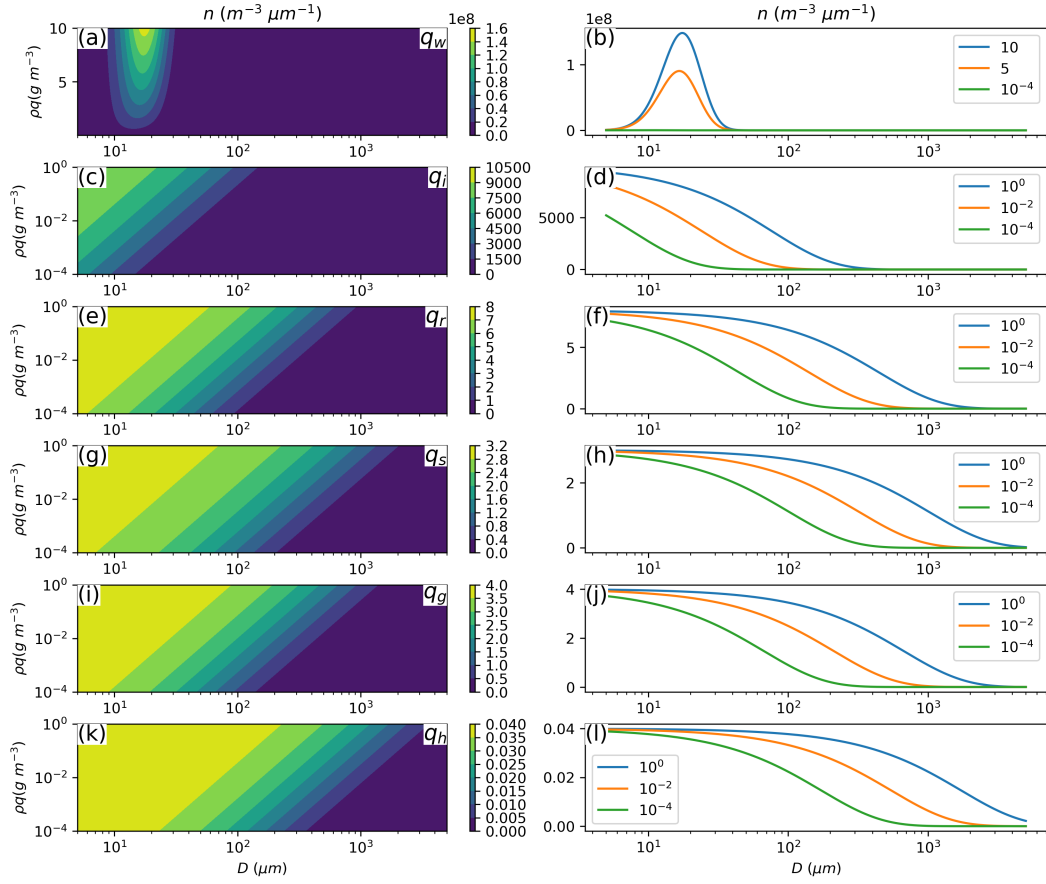


**Figure 1.** (a, c, e, g, i, k) Particle size distribution (PSD,  $n$ , unit:  $m^{-3} \mu m^{-1}$ ) as a function of diameter ( $D$ , unit:  $\mu m$ ) and cloud content ( $\rho q$ , unit:  $g m^{-3}$ ). (b, d, f, h, j, l) PSD as a function of diameter at three selected cloud water content amounts. (a) and (b) are cloud water ( $q_w$ ), (c) and (d) are cloud ice ( $q_i$ ), (e) and (f) are rain ( $q_r$ ), (g) and (h) are snow ( $q_s$ ), (i) and (j) are graupel ( $q_g$ ), and (k) and (l) are hail ( $q_h$ ).

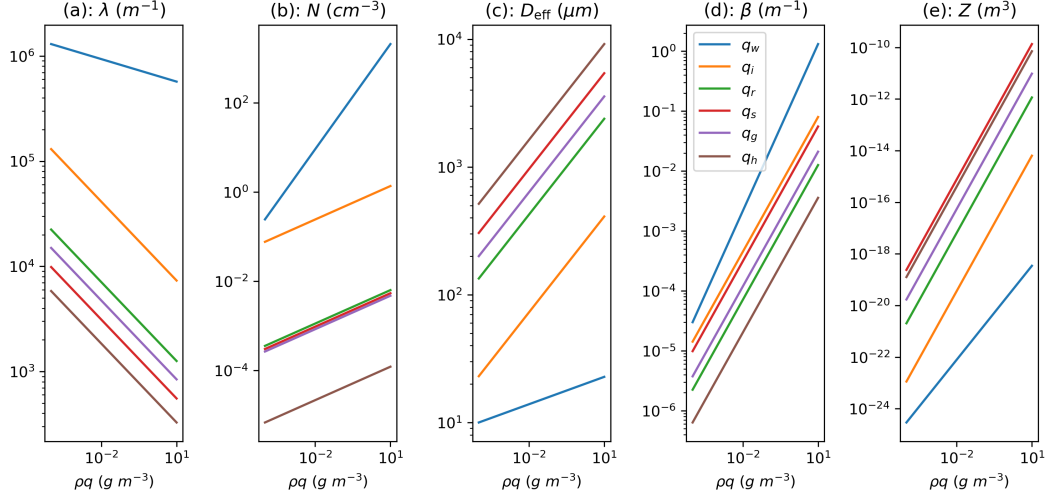


**Figure 2.** From left to right are the (a) slope parameter ( $\lambda$ , unit:  $m^{-1}$ ), (b) particle concentration ( $N$ , unit:  $cm^{-3}$ ), (c) effective diameter ( $D_{\text{eff}}$ , unit:  $\mu m$ ), (d) optical extinction ( $\beta$ , unit:  $m^{-1}$ ), and (e) radar reflectivity factor ( $Z$ , unit:  $m^3$ ) for each cloud category as a function of cloud content ( $\rho q$ , unit:  $g m^{-3}$ ). Blue, orange, green, red, purple, and brown lines are the quantities of cloud water ( $q_w$ ), cloud ice ( $q_i$ ), rain ( $q_r$ ), snow ( $q_s$ ), graupel ( $q_g$ ), and hail ( $q_h$ ).

$$Z = \int_0^{\infty} D^6 n(D) dD = \frac{n_0 \Gamma(\mu + 6)}{\lambda^{\mu+6}}. \quad (6)$$

The density ( $\rho_0$ ) of each cloud category is listed in Table 1.  $\rho$  is the density of air. In the single-moment case where the mass mixing ratio ( $q$ ) is a prognostic variable, the slope parameter ( $\lambda$ ) can be derived from Equation (5):

$$\lambda = \left[ \frac{\pi \rho_0 n_0 \Gamma(\mu + 3)}{6 \rho q} \right]^{1/(\mu+3)}. \quad (7)$$

By definition, and apparent from Figure 2, the slope parameter ( $\lambda$ ), particle concentration ( $N$ ), effective diameter ( $D_{\text{eff}}$ ), optical extinction ( $\beta$ ), and radar reflectivity factor ( $Z$ ) are all a power function of cloud content ( $\rho q$ ). As shown in Figure 2b, assuming the same cloud content, the particle concentration of cloud water is an order of magnitude larger than cloud ice and two orders of magnitude larger than rain, snow, and graupel. Hail is an order of magnitude less than graupel. The increment of cloud water particle concentration regarding cloud water content is about two orders larger than other cloud categories. As shown in Figure 2c, the effective diameter of cloud water is about  $10 \mu m$  to  $20 \mu m$ , and cloud ice is about  $20 \mu m$  to  $400 \mu m$ . The effective diameters of rain, graupel, snow, and hail are close, with the latter larger than the former. As shown in Figure 2d, the optical extinction of all cloud categories is quite close and similar to each other in tendency. Optical extinction is the largest for cloud water and the smallest for hail, with two orders of difference. As shown in Figure 2e, cloud water has the smallest radar reflectivity factor, but snow and hail have the largest.

We briefly describe how this method can be easily extended to a double-moment ( $DM$ ) scheme, in which both the particle concentration ( $N$ ) and mass mixing ratio ( $q$ ) are prognostic variables. The intercept parameter ( $n_0^{DM}$ ) and slope parameter ( $\lambda^{DM}$ ) can be derived from the combination of Equation (2) and (5):

$$n_0^{DM} = \frac{N^{1+\mu/3}}{\Gamma(\mu)} \left[ \frac{\pi \rho_0 \Gamma(\mu + 3)}{6 \rho q \Gamma(\mu)} \right]^{\mu/3}, \quad (8)$$

$$\lambda^{DM} = \left[ \frac{\pi \rho_0 N \Gamma(\mu + 3)}{6 \rho q \Gamma(\mu)} \right]^{1/3}. \quad (9)$$

In this case, the spectra shape parameter ( $\mu$ ) is the only variable that needs to be pre-defined or parameterized. For cloud water, following Morrison and Gettelman (2008), it is defined as:

$$\mu^{DM} = \frac{1}{(0.000571 N_c + 0.2714)^2}. \quad (10)$$

Where  $N_c$  (unit:  $cm^{-3}$ ) is the cloud droplet number concentration defined separately in different cloud scenario. When  $N_c$  equals to  $52.827 cm^{-3}$ ,  $\mu^{DM}$  is 11, the one that used in the current single-moment scheme. For cloud ice, following Morrison and Milbrandt (2015), it is defined as:

$$\mu^{DM} = 0.00191 (\lambda^{DM})^{0.8} - 2. \quad (11)$$

For all other cloud categories,  $\mu^{DM} = 1$ . The double-moment extension of the GFDL MP is still under development and is not used in this paper. However as shown here the double-moment scheme can be implemented as an extension of the current single-moment scheme, and serves as a reference for future GFDL MP development.

### 3.3 Terminal Velocity

Terminal velocity ( $V$ ) is generally given as a power-law relationship with respect to particle size (Straka, 2009):

$$V = \alpha D^\beta, \quad (12)$$

The leading coefficient  $\alpha$  and the power  $\beta$  for each cloud categories are listed in Table 1. The parameters for cloud water, cloud ice, rain, snow, and graupel or hail follow Ikawa and Saito (1991), McFarquhar et al. (2015), Liu and Orville (1969), Straka (2009), and Pruppacher and Klett (2010), respectively. The terminal velocity used in the microphysical processes can be weighted by number ( $V_N$ ), mass ( $V_M$ ), or even reflectivity ( $V_Z$ ) corresponding to each moment (Milbrandt & Yau, 2005). After applying the gamma distribution, the terminal velocities can be written as:

$$V_N = \frac{\int_0^\infty V n(D) dD}{\int_0^\infty n(D) dD} = \frac{\alpha \Gamma(\mu + \beta)}{\lambda^\beta \Gamma(\mu)}, \quad (13)$$

$$V_M = \frac{\int_0^\infty V D^3 n(D) dD}{\int_0^\infty D^3 n(D) dD} = \frac{\alpha \Gamma(\mu + \beta + 3)}{\lambda^\beta \Gamma(\mu + 3)}, \quad (14)$$

$$V_Z = \frac{\int_0^\infty V D^6 n(D) dD}{\int_0^\infty D^6 n(D) dD} = \frac{\alpha \Gamma(\mu + \beta + 6)}{\lambda^\beta \Gamma(\mu + 6)}. \quad (15)$$

Generally, the reflectivity weighted terminal velocity ( $V_Z$ ) is larger than the mass weighted terminal velocity ( $V_M$ ), which is further larger than the number weighted terminal velocity ( $V_N$ ) (Milbrandt & Yau, 2005). It can also be seen in Figure 3, the terminal velocity of cloud water is the smallest ( $\approx 0.01 m s^{-1}$ ), followed by cloud ice ( $\approx 0.1-0.7 m s^{-1}$ ), snow ( $\approx 0.5-2 m s^{-1}$ ), graupel ( $\approx 0.4-4 m s^{-1}$ ), rain ( $\approx 0.4-10 m s^{-1}$ ), and hail ( $\approx 0.7-20 m s^{-1}$ ). In the GFDL MP, the mass-weighted terminal velocity is used following Y. L. Lin et al. (1983), because the mass mixing ratio is the only prognostic moment. Note that unlike most microphysical schemes, including earlier versions of the GFDL MP, the GFDL MP v3 includes sedimentation of cloud water.

### 3.4 Microphysical Processes

Since the PSDs are redefined, many cloud microphysical processes are reformulated accordingly to ensure an overall microphysical consistency and easily permit introductions of new particle size distributions, microphysical processes, and multi-moment distributions. Those cloud microphysical processes include accretion, evaporation, sublimation, deposition, melting, and freezing derived initially based on the PSD.

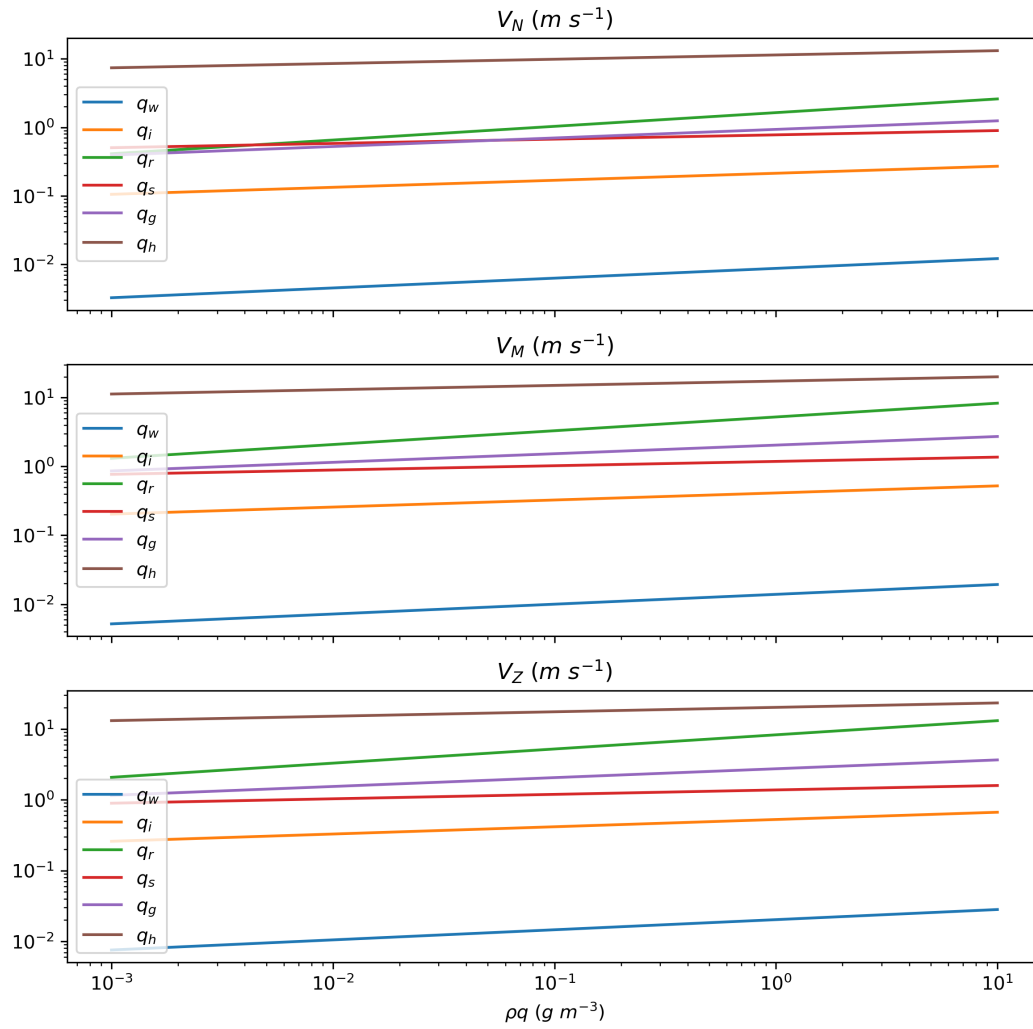


**Figure 3.** From top to bottom are the number weighted ( $V_N$ ), mass weighted ( $V_M$ ), and reflectivity weighted ( $V_Z$ ) terminal velocities (unit:  $m s^{-1}$ ) as a function of water content ( $\rho q$ , unit:  $g m^{-3}$ ). Blue, orange, green, red, purple, and brown lines are the terminal velocities of cloud water ( $q_w$ ), cloud ice ( $q_i$ ), rain ( $q_r$ ), snow ( $q_s$ ), graupel ( $q_g$ ), and hail ( $q_h$ ).

316 Accretion between each two falling cloud categories follows Wisner et al. (1972).  
 317 The accretion rate between cloud  $x$  and  $y$  ( $P_{xacy}$ , accretion of  $y$  by  $x$ , unit:  $kg\ kg^{-1}\ s^{-1}$ )  
 318 is reformulated after putting the gamma distribution in and integrating the particle size  
 319 from zero to infinity:

$$320 \quad P_{xacy} = \int_0^\infty \int_0^\infty \frac{\pi^2}{24} E_{xy} |V_x - V_y| \frac{\rho_{y0}}{\rho} (D_x + D_y)^2 D_y^3 n_x(D_x) n_y(D_y) dD_x dD_y$$

$$321 \quad = \frac{\pi^2}{24} E_{xy} n_{x0} n_{y0} |V_x - V_y| \frac{\rho_{y0}}{\rho} \left[ \frac{\Gamma(\mu_x) \Gamma(\mu_y + 5)}{\lambda_x^{\mu_x} \lambda_y^{\mu_y + 5}} + \frac{\Gamma(\mu_x + 2) \Gamma(\mu_y + 3)}{\lambda_x^{\mu_x + 2} \lambda_y^{\mu_y + 3}} + \frac{2\Gamma(\mu_x + 1) \Gamma(\mu_y + 4)}{\lambda_x^{\mu_x + 1} \lambda_y^{\mu_y + 4}} \right], \quad (16)$$

322 where  $V_x$  and  $V_y$  are the terminal velocities of cloud  $x$  and  $y$ , respectively.  $E_{xy}$  is the col-  
 323 lection efficiency between cloud  $x$  and  $y$ . Specifically,  $E_{rw} = 0.35$ ,  $E_{ri} = 1.0$ ,  $E_{sw} =$   
 324  $1.0$ ,  $E_{si} = 0.35$ ,  $E_{sr} = 1.0$ ,  $E_{gw}/E_{hw} = 1 \times 10^{-4}$ ,  $E_{gi}/E_{hi} = 0.05$ ,  $E_{gr}/E_{hr} = 1.0$ , and  
 325  $E_{gs}/E_{hs} = 0.01$ . This formula can be simplified when one of the two cloud categories  
 326 (e.g.,  $y$ ) does not fall and is distributed mono-dispersedly as:

$$327 \quad P_{xacy} = \int_0^\infty \frac{\pi}{4} E_{xy} q_y V_x D_x^2 n_x(D_x) dD_x = \frac{\pi E_{xy} n_{x0} \alpha_x q_y \Gamma(\mu_x + \beta_x + 2)}{4 \lambda^{\mu_x + \beta_x + 2}}, \quad (17)$$

328 The exponential case ( $\mu = 1$ ) of Equation (16) and (17) are widely used in the Y. L. Lin  
 329 et al. (1983) scheme and in early versions of the GFDL MP scheme.

330 Evaporation, sublimation and deposition follow Byers (1965). The evaporation /  
 331 sublimation / deposition rate ( $P_{ESD}$ , unit:  $kg\ kg^{-1}\ s^{-1}$ ) is reformulated after putting  
 332 the gamma distribution in and integrating the particle size from zero to infinity:

$$333 \quad P_{ESD} = \int_0^\infty \frac{2\pi(S-1)}{\rho(A+B)} V_f D n(D) dD = \frac{2\pi(S-1)}{\rho(A+B)} \frac{n_0 \Gamma(\mu+1)}{\lambda^{\mu+1}} V_f, \quad (18)$$

334 where  $S$  is the ratio between saturated mixing ratio of water vapor ( $q_{sat}$ ) and water va-  
 335 por mixing ratio ( $q_v$ ),  $A$  and  $B$  are thermodynamics terms defined as:

$$336 \quad A = \frac{L^2}{K_a R_v T^2}, \quad (19)$$

$$337 \quad B = \frac{1}{\rho q_{sat} \psi}, \quad (20)$$

338 where  $L$  is the latent heat coefficient,  $K_a = 2.36 \times 10^{-2}\ J\ m^{-1}\ s^{-1}\ K^{-1}$  is the ther-  
 339 mal conductivity of air,  $R_v$  is gas constant of water vapor,  $T$  is air temperature, and  $\psi =$   
 340  $2.11 \times 10^{-5}\ m^2\ s^{-1}$  is diffusivity of water vapor.

341 The ventilation coefficient ( $V_f$ ) in Equation (18) is defined followed Beard and Prup-  
 342 pachter (1971). After putting the gamma distribution in and integrating the particle size  
 343 from zero to infinity,  $V_f$  is reformatted as:

$$344 \quad V_f = 0.78 + 0.31 S_c^{1/3} \nu^{-1/2} \frac{\int_0^\infty V^{1/2} D^{3/2} n(D) dD}{\int_0^\infty D n(D) dD} = 0.78 + 0.31 S_c^{1/3} \nu^{-1/2} \frac{\alpha^{1/2} \Gamma\left(\mu + \frac{\beta+3}{2}\right)}{\lambda^{\mu + \frac{\beta+3}{2}}} \frac{\lambda^{\mu+1}}{\Gamma(\mu+1)}, \quad (21)$$

345 where  $\nu = 1.259 \times 10^{-5}\ m^2\ s^{-1}$  is the kinematic viscosity of air and  $S_c = \nu/\psi$  is the  
 346 Schmidt number.

347 The melting process follows Mason (1971). The melting rate ( $P_{melt}$ , unit:  $kg\ kg^{-1}\ s^{-1}$ )  
 348 is reformulated after putting the gamma distribution in and integrating the particle size  
 349 from zero to infinity:

$$350 \quad P_{melt} = \int_0^\infty \frac{2\pi}{\rho L} [K_a (T - T_0) - L\psi\rho(q_{sat} - q_v)] V_f D n(D) dD$$

$$351 \quad = \frac{2\pi}{\rho L} [K_a (T - T_0) - L\psi\rho(q_{sat} - q_v)] \frac{n_0 \Gamma(\mu+1)}{\lambda^{\mu+1}} V_f, \quad (22)$$

where  $T_0$  is the freezing temperature.

At last, the rain freezing process follows Wisner et al. (1972). The freezing rate ( $P_{fr}$ , unit:  $kg\ kg^{-1}\ s^{-1}$ ) is reformulated after putting the gamma distribution in and integrating the particle size from zero to infinity:

$$\begin{aligned} P_{fr} &= \int_0^\infty \frac{\pi^2}{36} D^6 \frac{\rho_0}{\rho} B' \exp[A'(T_0 - T) - 1] n(D) dD \\ &= \frac{\pi^2}{36} n_0 \frac{\rho_0}{\rho} B' \exp[A'(T_0 - T) - 1] \frac{\Gamma(\mu + 6)}{\lambda^{\mu+6}}, \end{aligned} \quad (23)$$

where  $A' = 0.66\ K^{-1}$  and  $B' = 100\ m^{-3}\ s^{-1}$  are two constant parameters following Bigg (1953).

The following microphysical processes remain the same from GFDL MP v2: 1) condensation and evaporation of cloud water, 2) deposition and sublimation of cloud ice, 3) cloud ice freezing and melting, 3) cloud water autoconversion, 5) cloud ice aggregation or autoconversion, 6) snow aggregation or autoconversion. Future GFDL MP development will include the particle size distribution to these remaining processes.

### 3.5 Cloud Condensation Nuclei

Among these microphysical processes, cloud water to rain autoconversion follows the equation (15) in Rotstayn (1997). In this process, the cloud droplet concentration is a key factor. The cloud droplet concentration in the current version of GFDL MP is an input parameter which is parameterized as a function of cloud condensation nuclei (CCNs). According to equation (15) in Rotstayn (1997), the more CCNs in the cloud, the slower is the cloud water to rain autoconversion. For simplicity, the CCNs in the GFDL MP v2 used two fixed values over the land and the ocean, respectively. The land value of  $300\ cm^{-3}$  is from Tripoli and Cotton (1980), while the ocean value of  $100\ cm^{-3}$  is from Rotstayn (1997). Therefore, the aerosol-related microphysical processes and the aerosol-cloud interactions may not be properly represented in the GFDL MP v2 due to unrealistic CCNs distribution.

In the GFDL MP v3 we instead use aerosol data in the Modern-Era Retrospective analysis for Research and Applications, version 2 (MERRA2) (Rienecker et al., 2011) from the National Aeronautics and Space Administration (NASA) Goddard Earth Science Data Information and Services Center (GES DISC). This aerosol product is one of the reanalyses from the Goddard Earth Observing System Model, Version 5 (GEOS-5) data assimilation system (Randles et al., 2017; Gelaro et al., 2017). We combined the 3-hourly aerosol data from 2015 to 2020 to create a 12-month climatological dataset consisting of 72 vertical levels from the surface to about 1.3 Pa at the top. The horizontal resolution is 0.5 by 0.625 degrees. The species of sulfate, which is a subset of MERRA2 aerosol, is converted to CCNs using Boucher and Lohmann (1995) formula before feeding in the GFDL MP v3.

Figures 4a,b show the geographic distribution of surface climatological CCNs derived from MERRA2 and its difference from the values used in the GFDL MP v2 ( $300$  and  $100\ cm^{-3}$  over the land and the ocean, respectively). Over most of the land area except southeastern China and northern India, the CCNs from MERRA2 is below  $300\ cm^{-3}$ . The CCNs over all of Antarctica is below  $100\ cm^{-3}$ . Over most of the ocean area except the offshore of Asia and Europe, the east coast of North America, and the northern Pacific Ocean, the CCNs from MERRA2 is below  $100\ cm^{-3}$ . Only the CCNs over the offshore of China and India can reach to above  $300\ cm^{-3}$ . This comparison indicates that the fixed values of CCNs used in the GFDL MP v2 are substantially overestimated over most of the global area. Besides the horizontal spatial variability, the CCNs from MERRA2 also has vertical variability. Figure 4c shows that the vertical mean distributions and ranges decrease with height and are much smaller than the fixed values used

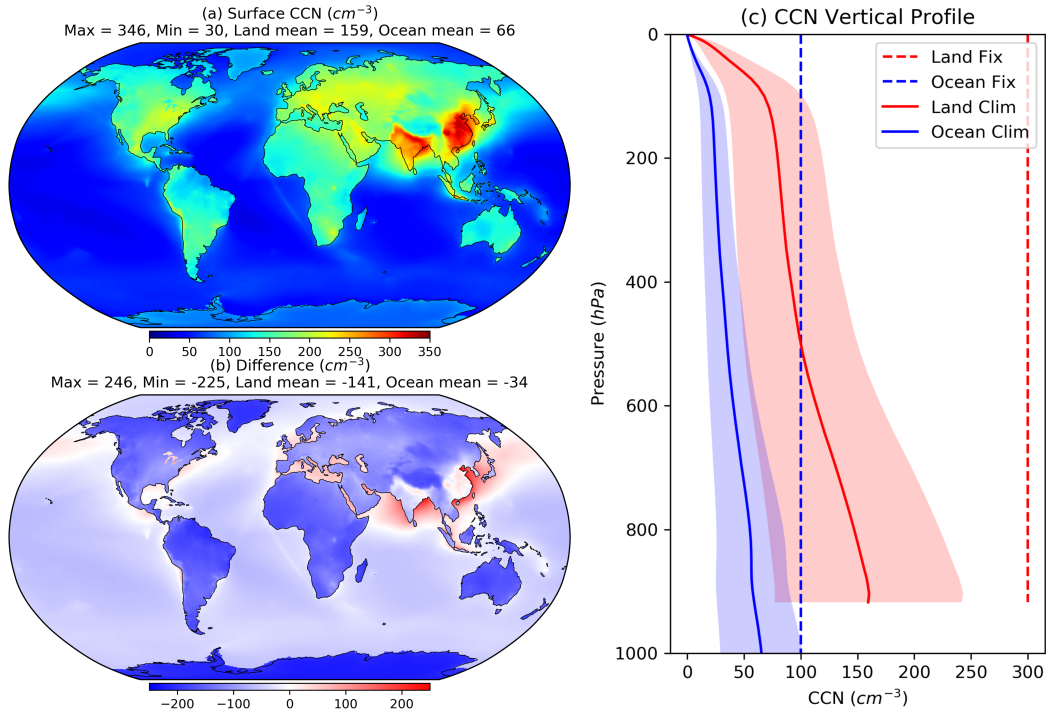


**Figure 4.** Geographic distribution of (a) surface climatological CCNs ( $cm^{-3}$ ) from MERRA2, (b) the difference between the CCNs from MERRA2 and the fixed CCNs values used in the GFDL MP v2. Panel (c) is the vertical profiles of (solid) climatological CCNs from MERRA2 and (dashed) fixed CCNs values used in the GFDL MP v2. Red lines represent CCNs over land, blue lines represent CCNs over the ocean. The shaded area is its standard deviation. The numbers in panels (a) and (b) are the global maximum, minimum, land mean, and ocean mean of CCNs.

400 in the GFDL MP v2. The CCN over land is only half of  $300\text{ cm}^{-3}$  near the surface and  
 401 lower than  $100\text{ cm}^{-3}$  above 500 hPa. The CCNs over the ocean is generally half value  
 402 or lower than the fixed value of  $100\text{ cm}^{-3}$ .

#### 403 **4 Model Verification**

404 In order to demonstrate the impact of the GFDL MP upgrade, 10-day weather prediction  
 405 from SHIELD are evaluated. These predictions are initialized from GFS v15 analyses every five  
 406 days from June 25, 2019 to March 17, 2021. The ERA5 reanalysis (Hersbach  
 407 et al., 2020) is then used for global weather prediction evaluation. ERA5 is produced using  
 408 4D-Var data assimilation and model forecasts in CY41R2 of the European Centre  
 409 for Medium-Range Weather Forecasts (ECMWF) Integrated Forecast System (IFS), with  
 410 137 hybrid sigma/pressure (model) levels in the vertical and the top-level at 0.01 hPa.  
 411 Here the 31 km 6 hourly ERA5 datasets at the pressure levels of 100 hPa, 200 hPa, 250  
 412 hPa, 500 hPa, 700 hPa, 850 hPa, and 1000 hPa are used to represent the weather and  
 413 atmospheric condition from Tropopause to the surface. Here we focus on geopotential  
 414 height, air temperature, and specific humidity, which are of the greatest value to large-  
 415 scale weather prediction. All experiments done for this study are listed in Table 2. This  
 416 section compares the GFDL MP v3 (CTRL for short hereafter; this configuration uses  
 417 constant CCNs over the land and ocean respectively and the original PSD for all cloud

**Table 2.** List of experiments in this study.

Experiment	Old PSD <sup>1</sup>	Old CCNs <sup>2</sup>	New PSD <sup>3</sup>	New CCNs <sup>4</sup>	GFDL MP
OLD	×	×			v2
CTRL	×	×			v3
CPSD		×	×		v3
AERO	×			×	v3
CPSD_AERO			×	×	v3

<sup>1</sup> mono-dispersed for cloud water and cloud ice, exponential distribution for other cloud categories. <sup>2</sup>  $300 \text{ cm}^{-3}$  over land and  $100 \text{ cm}^{-3}$  over ocean. <sup>3</sup> gamma distribution for all cloud categories. <sup>4</sup> CCNs are calculated from climatological aerosol.

418 categories) with the GFDL MP v2 (OLD for short hereafter). In the following section,  
 419 the CTRL is used as a reference to evaluate the weather prediction skill of the GFDL  
 420 MP v3. CTRL is compared against simulations with the more realistic gamma particle  
 421 size distribution of cloud water and cloud ice (CPSD), a time-and-space varying clima-  
 422 tological background aerosol for CCNs calculation (AERO), and simulations with both  
 423 (CPSD\_AERO).

424 Figure 5 shows a straightforward comparison between the OLD and the CTRL us-  
 425 ing a scorecard. The scorecard clearly shows that the CTRL has significantly higher anomaly  
 426 correlation coefficients (ACCs) of geopotential height at most pressure levels up to seven  
 427 days of forecast. The reduction of geopotential height bias from the OLD to the CTRL  
 428 is significant even throughout the ten days of forecast. Although the ACCs of the CTRL  
 429 are lower than those of the OLD after day seventh, this difference is insignificant. The  
 430 above improvement of geopotential height prediction (higher ACC of geopotential height)  
 431 is encouraging for the development of SHiELD because it indicates a general improve-  
 432 ment of the atmospheric circulation and heating in the Troposphere, which is closely re-  
 433 lated to our daily weather. It is also found in Figure 5 that the temperature prediction  
 434 of the CTRL is overall better than the OLD. Still, the ACCs are higher in the first few  
 435 days and lower in the eight to ten-day forecast, while the bias is significantly reduced  
 436 throughout the ten-day forecast. Unfortunately, temperature prediction at 500 hPa and  
 437 1000 hPa are degraded in the CTRL (lower ACC and larger bias). Further analyses on  
 438 the 10-day temperature evolution and its 10-day averaged geographical distribution (see  
 439 supplemental Figures S1, S2) show a globally warm bias at 500 hPa and 1000 hPa. Since  
 440 the CTRL predicts an overall warmer Troposphere than the OLD and the 500 hPa and  
 441 1000 hPa temperature in the OLD already have a positive bias, the additional warm-  
 442 ing further increases the positive bias at these two pressure levels. Specific humidity pre-  
 443 diction is overall better at the upper Troposphere but worse at the lower Troposphere  
 444 comparing the CTRL to the OLD, shown in the scorecard. However, compared to the  
 445 magnitude and variation of specific humidity throughout the ten days of forecasts, their  
 446 difference at the lower Troposphere is small, so that can be negligible (see supplement-  
 447 al Figures S1, S2).

448 To evaluate the representation of the mean state of cloud prediction, we compare  
 449 the output from COSP (Cloud Feedback Model Intercomparison Project Observation  
 450 Simulator Package, Bodas-Salcedo et al. (2011); Swales et al. (2018)) of SHiELD against  
 451 CALIPSO (Cloud-Aerosol Lidar and Infrared Pathfinder Satellite Observation, Chepfer  
 452 et al. (2010)) cloud fraction product. The COSP takes the models representation of the  
 453 atmosphere (e.g., cloud water content at model levels) and simulates the retrievals for  
 454 several passive and active sensors (e.g., CALIPSO) (Bodas-Salcedo et al., 2011). The out-  
 455 put from COSP can then be directly compared with satellite observations. Version 2 of  
 456 COSP (Swales et al., 2018), a significant reorganization and modernization of the pre-



457 various generation of COSP, has been recently implemented into SHIELD for comprehen-  
 458 sive cloud evaluation. The CALIPSO data is from the GCM-Oriented CALIPSO Cloud  
 459 Product (CALIPSO-GOCCP) [https://climserv.ipsl.polytechnique.fr/cfmip-obs/  
 460 Calipso-goccp.html](https://climserv.ipsl.polytechnique.fr/cfmip-obs/Calipso-goccp.html) that is designed to evaluate GCM (General Circulation Model) cloudi-  
 461 ness. CALIPSO-GOCCP (Chepfer et al., 2010) contains observational cloud diagnostics  
 462 entirely consistent with the ones simulated by the ensemble "GCM+lidar simulator" which  
 463 has been built in using the same horizontal and vertical resolutions and the same cloud  
 464 detection thresholds. The lidar simulator is part of COSP. In this study, the total col-  
 465 umn cloud liquid water, rainwater, cloud ice water, and snow water from ERA5 is also  
 466 used to evaluate the liquid and ice water paths predicted in SHIELD. Note that graup-  
 467 pel is not included in ERA5. Here, total column cloud liquid water and rainwater are  
 468 combined as liquid water path, and total column cloud ice water and snow water are com-  
 469 bined as ice water path. Finally, precipitation prediction is evaluated against the Inte-  
 470 grated Multi-satellitE Retrievals for GPM (IMERG) product (Hong et al., 2004), which  
 471 combines information from the Global Precipitation Measurement (GPM) satellite con-  
 472 stellation to estimate precipitation over the majority of the Earth's surface.

473 Figure 6 shows the cloud fraction comparison between model prediction and CALIPSO  
 474 observation. As shown in Figure 6e, the OLD predicts similar geographical distribution  
 475 and magnitude of high cloud fraction as CALIPSO. The predicted global mean high cloud  
 476 fraction is slightly smaller than that of the CALIPSO (with a bias of -0.006). As shown  
 477 in Figure 6i, the global mean bias further reduces to 0.001 (positive) in the CTRL, but  
 478 the root-mean-square error (rmse) remains the same. It can be found in the high cloud  
 479 fraction difference panel (Figure 6m) that a significant difference in high cloud fraction  
 480 is over the tropics ocean area. Different from the high cloud fraction, both middle and  
 481 low cloud fractions are under-predicted in both the OLD and the CTRL (Figure 6f,g,j,k).  
 482 As shown in Figure 6f,j, the predicted middle cloud fraction is consistently lower in the  
 483 model than CALIPSO, with a maximum reduction of cloud fraction over Southern Amer-  
 484 ica. Comparing the OLD and the CTRL, the upgrade of GFDL MP does not improve  
 485 the middle cloud fraction prediction too much. Still, the global mean bias and rmse of  
 486 the predicted middle cloud fraction are both reduced. As shown in Figure 6n, most of  
 487 the significant middle cloud fraction increment is in the middle to high latitude ocean  
 488 area, especially the Southern Ocean. Compared to the middle cloud fraction bias, the  
 489 low cloud fraction bias is even larger (Figure 6g,k). The global mean bias of low cloud  
 490 fraction is -0.194 and -0.197 in the OLD and the CTRL, respectively. As shown in Fig-  
 491 ure 6o, most significant reduction of low cloud fraction in the CTRL is over the high lat-  
 492 itude land area. Due to the under-prediction of middle and low cloud fractions, the to-  
 493 tal cloud fraction is also under-predicted (Figure 6h,i). Still, we can see that the global  
 494 mean bias and rmse of total cloud fraction is reduced because of significant total cloud  
 495 increment over the Southern Ocean (Figure 6p).

496 We further evaluate the liquid and ice water paths (compared with ERA5) and pre-  
 497 cipitation (compared with GPM) predictions. As shown in Figure 7a,d,g, SHIELD's pre-  
 498 dicted liquid water path is quite similar to ERA5 regarding its geographical distribution.  
 499 However, both the OLD and the CTRL over-predict the liquid water path over the extra-  
 500 tropical storm track area. Compared with the OLD, the bias and rmse in the CTRL are  
 501 both notably reduced. As shown in Figure 7j, most of the significant reduction of liq-  
 502 uid water path is at the middle to high latitudes, where the model over-predicts the liq-  
 503 uid water path. Compared with the ERA5, the geographical distributions of the ice wa-  
 504 ter path are well-predicted in both the OLD and the CTRL (Figure 7b,e,h). The bias  
 505 and rmse of the CTRL are only slightly smaller than that of the OLD. Not surprisingly,  
 506 the difference between the OLD and the CTRL is insignificant, shown from the differ-  
 507 ence panel of Figure 7k. Regarding the precipitation forecasts (Figure 7f,i), both the OLD  
 508 and the CTRL can well-predict the massive precipitation rates along the Intertropical  
 509 Convergence Zone (ITCZ) area and in the extra-tropical storm track area. However, both  
 510 the OLD and the CTRL predict slightly more precipitation globally, indicated by their

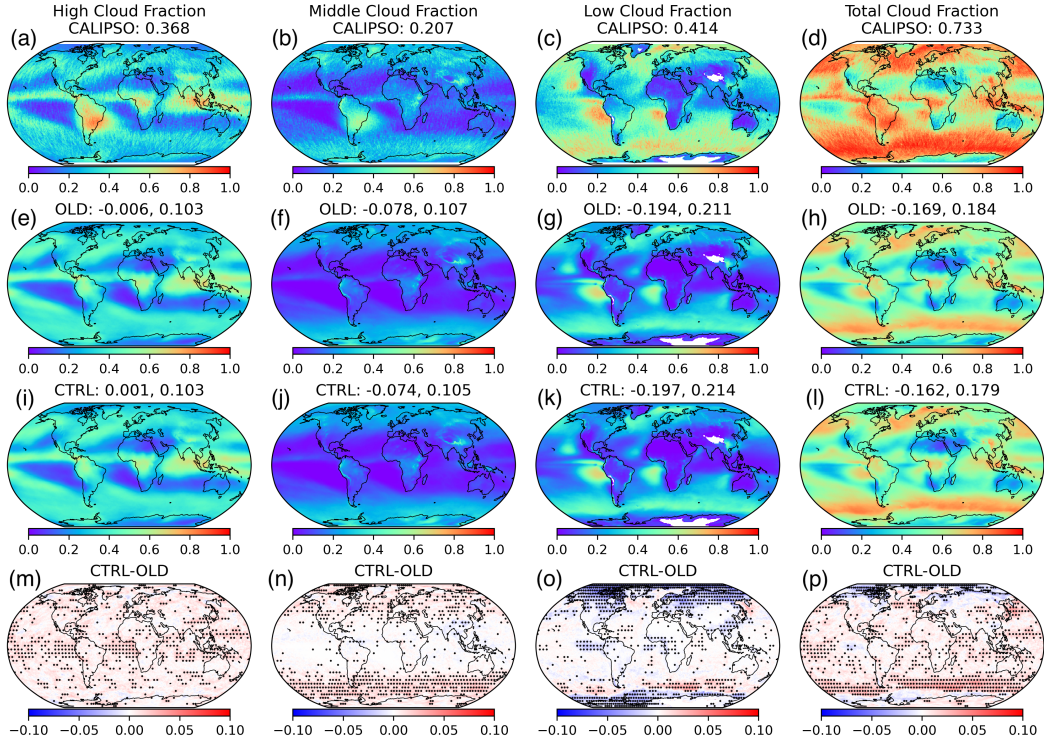


**Figure 6.** From left to right are the 10-day averaged high, middle, low, and total cloud fractions from (a-d) CALIPSO, (e-h) OLD, (i-l) CTRL, and (m-p) CTRL minus OLD. The numbers in the title of (a-d) are the global mean of cloud fraction (unit: 1), and (e-l) are the bias and root-mean-square error compared to CALIPSO. The dotted area in (m-p) is the area with a 95% significant difference.

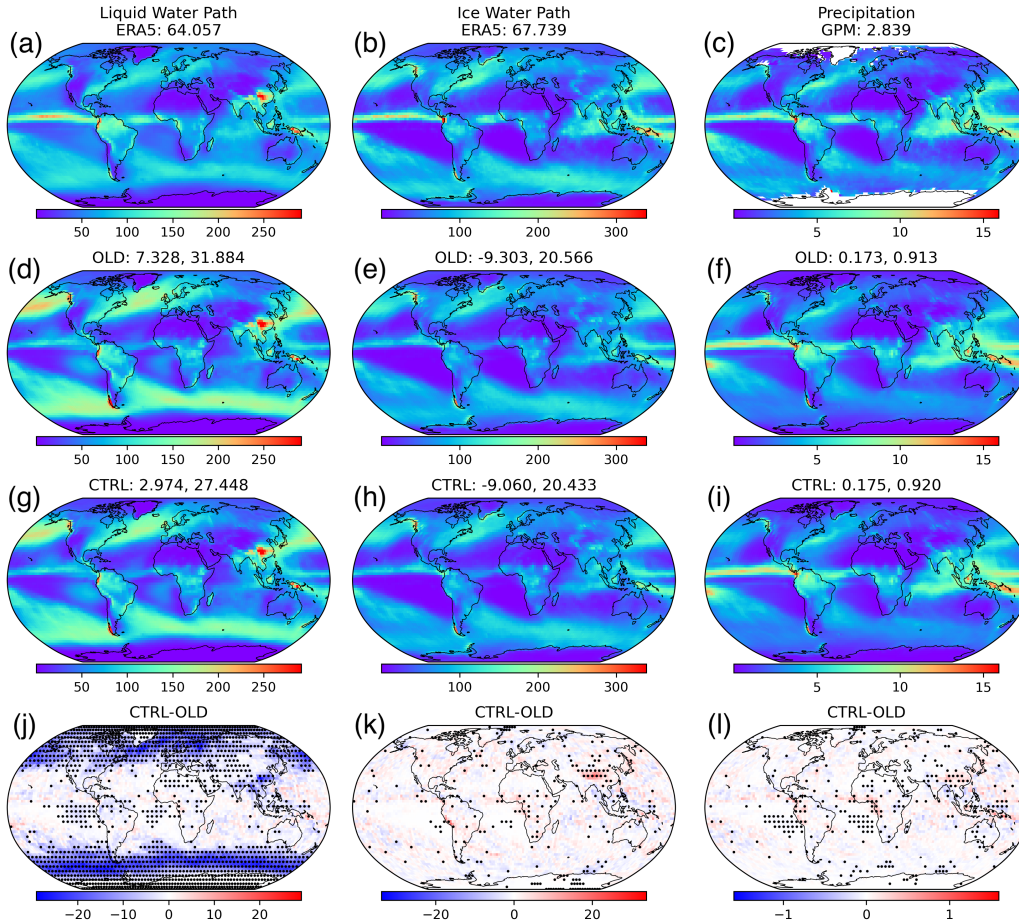


**Figure 7.** From left to right are the 10-day averaged liquid water path (LWP), ice water path (IWP), and precipitation rate (PRE) from (a-c) ERA5 or GPM, (d-f) OLD, (g-i) CTRL, and (j-l) CTRL minus OLD. The numbers in the title of (a-c) are the global mean of liquid water path or ice water path (unit:  $g m^{-2}$ ) or precipitation (unit:  $mm day^{-1}$ ), and (d-i) are the bias and root-mean-square error to ERA5 or GPM. The dotted area in (j-l) is the area with a 95% significant difference.

511 global mean bias. The CTRL's precipitation prediction has a slightly larger bias and rmse  
 512 than the OLD, but the differences are insignificant (Figure 7l).

## 5 Impacts of PSD and CCNs on Weather Prediction

513  
 514 The previous section demonstrates the results from the GFDL MP upgrade that  
 515 excludes the more realistic particle size distribution (PSD) and new cloud condensation  
 516 nuclei (CCNs). In the CTRL, the PSD of cloud water and cloud ice is still mono-dispersed,  
 517 and the CCNs are constant values over land and ocean separately. CTRL generally im-  
 518 proves the prediction skill of geopotential height and reduces biases in height, temper-  
 519 ature, and liquid water path, but had relatively little change to cloud biases. In this sec-  
 520 tion, three sensitivity experiments (CPSD, AERO, and CPSD\_AERO) are carried out to  
 521 evaluate the impacts (or effect) of the PSD in the GFDL MP v3, as well as the use of  
 522 time-and-space varying prescribed climatological aerosol to calculate CCNs, on weather  
 523 prediction. Those new experiments are listed in Table 2. Experiment CPSD is designed

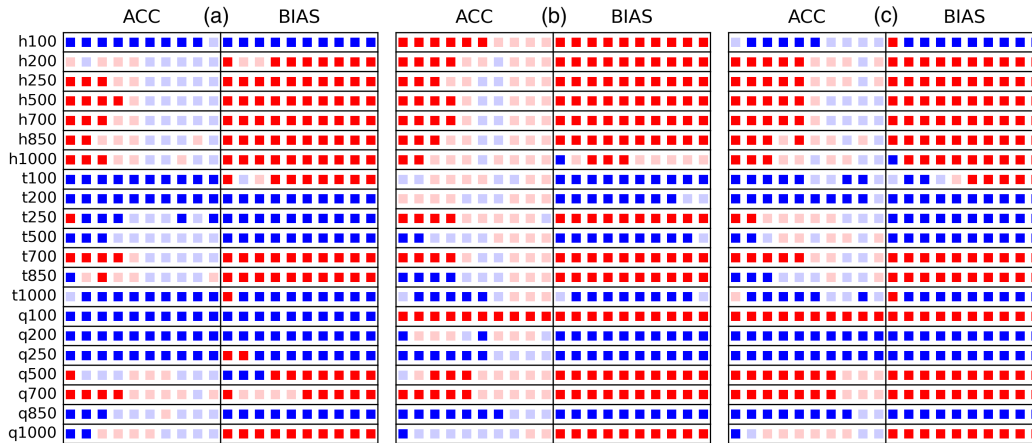


**Figure 8.** Similar to Figure 5, but for comparison between (a) CTRL and CPSD, (b) CTRL and AERO, (c) CTRL and CPSD\_AERO.

524 based on the CTRL with a more realistic PSD of cloud water and cloud ice using the  
 525 gamma distribution. Terminal velocity, effective radius, and a number of microphysical  
 526 processes are revised accordingly, as described in Section 3. Experiment AERO is also  
 527 designed based on the CTRL, but with the CCNs replaced with those calculated from  
 528 the MERRA2 climatological aerosol. CCNs are mainly used for cloud water to rainwa-  
 529 ter autoconversion in the GFDL MP. The last experiment is a combination of the CPSD  
 530 and the AERO experiments, called the CPSD\_AERO. Comparisons between the CTRL  
 531 and each of the three experiments use ERA5, CALIPSO, and GPM mentioned in the  
 532 previous section.

533 The scorecards of the comparison between the CTRL and each of the sensitivity  
 534 experiments are in Figure 8. It can be found that the ACCs of geopotential height in the  
 535 CPSD are higher than those in the CTRL in the first five-day forecast. Meanwhile, com-  
 536 pared to the CTRL, the biases of geopotential height prediction are significantly smaller  
 537 throughout the ten-day forecast (Figure 8a). On the other hand, the temperature and  
 538 specific humidity predictions in the CPSD are generally improved at levels lower than  
 539 500 hPa but significantly degraded at 500 hPa and above. The differences of the tem-  
 540 perature ACC between the CPSD and CTRL are hard to quantify in the time evolution  
 541 plots, but their difference of temperature biases are quite clear (see supplemental Fig-  
 542 ure S3). Compared to the CTRL, the predicted temperature in the CPSD is lower at  
 543 200 and 250 hPa, but higher at 500 hPa, and the predicted specific humidity in the CPSD  
 544 is lower at 100, 200, and 250 hPa.

545 To understand why the temperature and specific humidity decrease at the middle  
 546 to upper Troposphere (except that temperature at 500 hPa increases) in the CPSD than  
 547 the CTRL, we first examine the cloud fraction prediction (Figure 9). The CPSD pre-  
 548 dicted a similar amount of high cloud fraction to the CTRL (Figure 9e). The high cloud  
 549 fraction prediction bias is very close between the CPSD and the CTRL. The rmse of the  
 550 high cloud fraction prediction in the CPSD is slightly larger than that of the CTRL through-  
 551 out the ten-day forecast (Figure 9a). In contrast, there is a much more significant in-  
 552 crement of the rmse of middle cloud fraction prediction from the CTRL to the CPSD  
 553 (Figure 9b). Comparing the bias of middle cloud fraction prediction shown in Figure 9f,  
 554 we can see the predicted middle cloud fraction is significantly more in the CPSD than  
 555 the CTRL. It implies that more water vapor deposited to cloud ice to form middle clouds  
 556 in the CPSD. The associated latent heating warms up the air in the middle Troposphere.

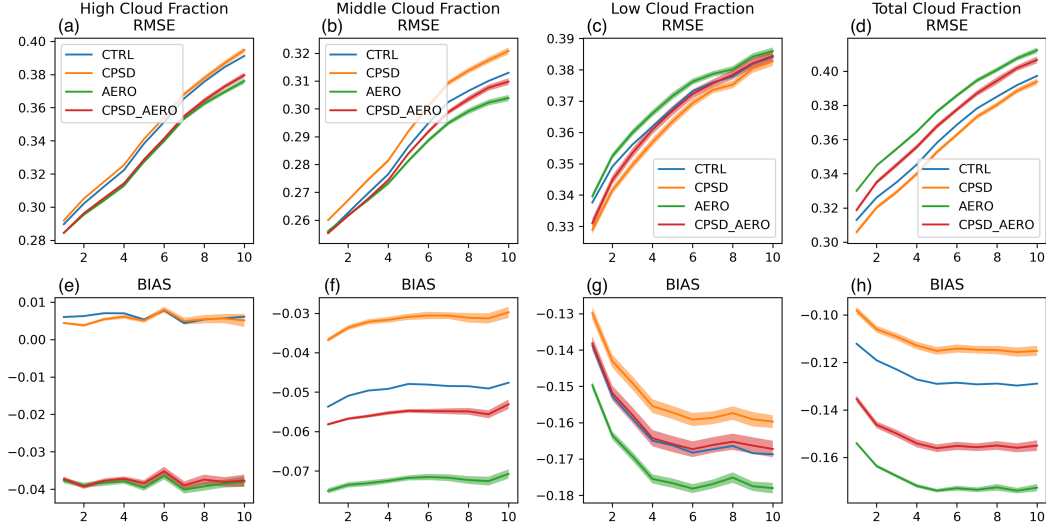


**Figure 9.** From left to right are the 10-day evolution of (a,e) high, (b,f) middle, (c,g) low, and (d,h) total cloud fractions of (blue) CTRL, (orange) CPSD, (green) AERO, and (red) CPSD\_AERO. Top row is root mean square error (unit: 1); bottom row is bias (unit: 1). The shaded area is the area with a 95% significant difference to the CTRL.

557 Due to the decrease of the water vapor in the upper Troposphere, the longwave radiation  
 558 absorption reduces; meanwhile, the increasing middle cloud fraction enhances the  
 559 cloud top cooling in the above air, the atmospheric temperature is decreased in the CPSD  
 560 compared to the CTRL. These are consistent with what we found in the temperature  
 561 and specific humidity prediction in Figure 8a.

562 The increases of the predicted cloud ice in the CPSD are also shown by the ice water  
 563 path (Figure 10e). The ice water path prediction bias changes from negative to positive  
 564 from the CTRL to the CPSD. The absolute ice water path prediction bias is relatively  
 565 smaller in the CPSD compared to the CTRL. However, the rmse of ice water path  
 566 prediction increases significantly (Figure 10b). The predicted ice water path dramati-  
 567 cally increases from the CTRL to the CPSD because of the increases of the cloud ice ter-  
 568 minal fall velocity in the CPSD with the redefinition of cloud ice PSD. As a result, it  
 569 brings more cloud ice sediment to lower levels, while the reduction of cloud ice at higher  
 570 levels causes more deposition of water vapor. The improvement of low cloud fraction pre-  
 571 diction (Figure 9c,g) probably contributes to the improvement of the temperature and  
 572 specific humidity prediction in the lower Troposphere (Figure 8a). The degradation of  
 573 the precipitation prediction is small in CPSD (Figure 10c,f).

574 The upgrade of the CCNs calculation in the AERO directly affects the autocon-  
 575 version of cloud water to rainwater. Figure 8b shows that the prediction skill of geopo-  
 576 tential height, temperature, and specific humidity are generally improved. Particularly,  
 577 the ACCs of geopotential height substantially increase with significant bias reductions.  
 578 Due to less produced CCNs in the AERO than the CTRL, it is relatively easier for the  
 579 cloud water to convert to rain and fall to the surface in the AERO than in the CTRL.  
 580 Therefore, the low cloud fraction in the AERO is largely reduced (Figure 9g), and the  
 581 liquid water path is also significantly reduced (Figure 10d). The reduction of cloud frac-  
 582 tion and the resultant reduced cloud albedo lead to a warmer surface. With a stronger  
 583 surface heat exchange, the lower Troposphere is warmed up. Extra heat is transported  
 584 from the lower Troposphere to the air above, inducing a warmer middle to upper Tro-  
 585 posphere. It is relatively harder for the water vapor to condense or deposit in the warmer

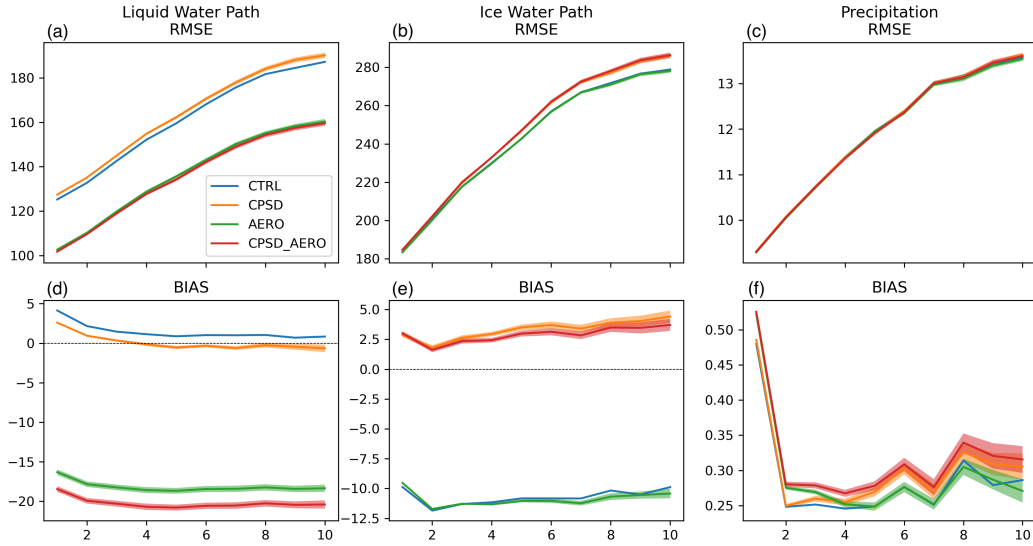


**Figure 10.** From left to right are the 10-day evolution of (a,d) liquid water path, (b,e) ice water path, and (c,f) precipitation of (blue) CTRL, (orange) CPSD, (green) AERO, and (red) CPSD\_AERO. Top row is root mean square error (unit:  $g m^{-2}$ ); bottom row is bias (unit:  $g m^{-2}$ ). The shaded area is the area with a 95% significant difference to the CTRL.

586 air. Therefore, the high and middle cloud fractions (Figure 9e, f) further decrease. Even  
 587 with more cloud water to rain autoconversion in the AERO than the CTRL, the changes  
 588 of precipitation prediction are still minor (Figure 10c,f), which may be related to some  
 589 compensation from the increase of convective precipitation.

590 Finally, the impacts of combining the more realistic PSD and the climatological aerosol  
 591 calculated CCNs are evaluated (Exp. of CPSD\_AERO). Figure 8c shows that the AERO  
 592 can improve the degradation of the forecast skill shown in the CPSD. For example, the  
 593 forecasts of the geopotential height of the CPSD\_AERO during the first 5 days are sig-  
 594 nificantly improved compared to the CTRL. Moreover, temperature forecasts at 250 and  
 595 500 hPa, and forecasts of specific humidity at 100, 500, and 700 hPa are generally im-  
 596 proved in the CPSD\_AERO. Generally speaking, there are more improved forecast fields  
 597 than degraded ones in the CPSD\_AERO than in the CTRL (Figure 8c). It is interest-  
 598 ing to find in Figure 9 that the high cloud fraction prediction in the CPSD\_AERO is quite  
 599 close to the AERO, but the middle, low, and total cloud fraction prediction in the CPSD\_AERO  
 600 is in between the CPSD and the AERO. Differently, the prediction of the liquid water  
 601 path of the CPSD\_AERO is close to the AERO, but the ice water path of the CPSD\_AERO  
 602 is close to the CPSD. Since the update of the PSD alters many microphysical processes,  
 603 but the update of the CCNs changes the cloud water to rainwater autoconversion only,  
 604 it is difficult to explain these interesting findings. We leave these to further research.

605 In all experiments, we find that the change of PSD in the cloud water and the cloud  
 606 ice or the use of climatological aerosol for CCNs calculation only exerts a minor impact  
 607 on the precipitation prediction (Figure 10c,f). It is possibly due to the change of large-  
 608 scale precipitation being small compared to the change of cloud content. In addition, the  
 609 change of the large-scale precipitation could be compensated by an increase in convective  
 610 precipitation. Additionally, precipitation can be influenced by microphysical processes  
 611 that do not involve the change of PSD and CCNs.

## 6 Summary and Discussion

This paper documents the third version of the Geophysical Fluid Dynamics Laboratory cloud microphysics scheme (GFDL MP v3) that is upgraded from the previous versions of the GFDL MP used in the Global Forecast System (GFS), the System for High-resolution prediction on Earth-to-Local Domains (SHIELD), and a broader community through the Unified Forecast System (UFS). Compared with the GFDL MP v2, the GFDL MP v3 is featured with the following upgrades: 1) the code has been reorganized, optimized, and modularized by functions; 2) the particle size distribution used in the scheme for all six cloud categories are redefined as gamma distribution; 3) particle concentration, effective diameter, optical extinction, mass mixing ratio, radar reflectivity factor, and terminal velocity are all redefined based on the gamma distribution; 4) accretion, evaporation, sublimation, deposition, melting, and freezing microphysical processes are all reformulated based on the gamma distribution; 5) replacing uniform cloud condensation nuclei (CCNs) with climatological aerosols calculated from Modern-Era Retrospective analysis for Research and Applications, version 2 (MERRA2). The GFDL MP v3 ensures an overall microphysical consistency and easily permits the future introduction of new particle size distributions, microphysical processes, and multi-moment distributions.

The impacts of the GFDL MP upgrade item 1) on global weather, cloud, and precipitation predictions in SHIELD are comprehensively evaluated. The comparisons between the two sets of experiments show that GFDL MP v3 significantly improves the geopotential height prediction up to seven days on anomaly correlation coefficient (ACC) and throughout ten-day forecast on the bias. Improvement of geopotential height prediction indicates general improvement of the atmospheric circulation and heating in the Troposphere. The temperature prediction is overall better in GFDL MP v3 than in GFDL MP v2. The specific humidity prediction is overall better in GFDL MP v3 than GFDL MP v2 in the upper Troposphere but worse in the lower Troposphere. High, middle, and total cloud fractions predictions are improved in GFDL MP v3. Low cloud fraction prediction degrades in GFDL MP v3, but liquid water path prediction improves substantially. There is a minor change in the ice water path and precipitation prediction from GFDL MP v2 and GFDL MP v3. It is believed that the noticed degradation could be improved with further model development.

Furthermore, the impacts of the GFDL MP upgrade items 2) to 5) are evaluated using the base GFDL MP v3 as a reference. The use of more realistic PSD and climatological aerosol calculated CCNs significantly improves the geopotential height prediction compared with the original PSD and constant CCNs. Temperature and specific humidity predictions at the upper Troposphere significantly degrade with the PSD upgrade, but are mixed with improvement and degradation with the CCNs upgrade. Among all upgrades, the PSD upgrade shows the best prediction of low and total cloud fractions but the worst prediction of high and middle cloud fractions, while the CCNs upgrade shows the best prediction of high and middle cloud fractions but the worst prediction of low and total cloud fractions. The combination of the PSD and the CCNs upgrades is generally excellent in cloud fraction prediction. The combination of the PSD and the CCNs upgrades shows the best liquid water path prediction with the lowest rmse, but with a very large negative bias. The PSD upgrade shows the largest rmse of liquid water path prediction, although its bias is the smallest. In contrast, the combination of the PSD and the CCNs upgrades shows the smallest bias in ice water path prediction but a larger rmse of the ice water path prediction. These results indicate that the global mean liquid and ice water paths are very different between the ERA5 and SHIELD. Note that we use ERA5 to evaluate liquid water path and ice water path prediction because this is the only reliable validation dataset available for the entire forecast time period. More reliable direct observations will be used for this purpose in the future.

664 There are some caveats for the GFDL MP v3. For example, the prediction of 500  
 665 hPa temperature tends to be worse (lower ACC and larger warm bias) than the GFDL  
 666 MP v2. This bias has been identified in SHiELD for a long time. A possible reason is  
 667 that the convective heating of the middle Troposphere is too strong, and radiative cool-  
 668 ing is not enough to compensate. Further investigation is still needed to alleviate this  
 669 bias. Middle, low, and total cloud fractions are under-predicted in SHiELD regardless  
 670 of the version of the GFDL MP used. We plan to extend our cloud fraction diagnosis  
 671 in the GFDL MP to include sub-grid terrain and static energy to better represent sub-  
 672 grid variability especially over complex terrain. We are also working on a more physically-  
 673 motivated definition of parameters in the particle size distribution using observations from  
 674 flights and to incorporate the effects of temperature, wind, and pressure on the PSD. This  
 675 aims to create a more realistic relationship between meteorological fields and particle size  
 676 distribution from observational data, and to resolve the degradation of upper-tropospheric  
 677 biases in temperature and humidity. We also plan to eliminate the low bias in low-to-  
 678 middle latitudes, and high bias in high latitudes, of liquid water path, and to improve  
 679 the seamlessness of the GFDL MP across space and time scales, as appropriate for the  
 680 wide range of applications of SHiELD, GFS, and UFS from convective-scale to seasonal  
 681 prediction. We also will consider a double-moment extension of the GFDL MP if it im-  
 682 proves the model's prediction skill.

### 683 **Appendix A The GFDL Cloud Microphysics Version 3**

684 The third version of the GFDL cloud microphysics scheme (GFDL MP) was de-  
 685 veloped from version 1 (Zhou et al., 2019) and version 2 (L. Harris, Zhou, Lin, et al., 2020).  
 686 This new version of the GFDL MP features with three major upgrades: 1) the code is  
 687 entirely reorganized, optimized, and modularized by functions, 2) there are various sci-  
 688 entific modifications to the microphysical processes, and 3) several optional definitions  
 689 and microphysical processes are added. The scientific modifications are summarized as  
 690 below:

- 691 • Redefine the supersaturation in ice processes using the complete saturation tables  
 692 (it is advance and ensures consistency);
- 693 • Allow cloud water autoconversion in a larger temperature range (it is consistent  
 694 with the temperature range of cloud water);
- 695 • Split rain evaporation and accretion more physically and consistently (it more phys-  
 696 ically handles the relation between rain evaporation and accretion);
- 697 • Turn off the redundant cloud ice melting before falling (the same process is already  
 698 in the ice microphysics section);
- 699 • Fix and revise the cloud ice melting processes during sedimentation (a bug was  
 700 found in these processes, not used by default);
- 701 • Remove several unnecessary temperature limits and add necessary mass limits (some  
 702 temperature limits are reasonably defined; mass limits prevent negative cloud mass)
- 703 • Use the same minimum value for all hydrometeors (to be consistent);
- 704 • Recalculate the parameters for terminal fall (for better precision and ease for fu-  
 705 ture development);
- 706 • Allow zero fall speed (instead of a small value; it is more physical);
- 707 • Remove time step splitting between fast saturation adjustment and full microphysics  
 708 (it is more reasonable in the current structure);
- 709 • Combine snow and graupel for snow effective radius diagnosis (to include the ra-  
 710 diative effect of graupel);
- 711 • When it is cloud water saturation adjustment, do it completely (by design).

712 There are also many options added to the GFDL MP that can be used in other appli-  
 713 cations of SHiELD (T-SHiELD, C-SHiELD, and S-SHiELD), toward unified modeling

714 in which there is a single modeling system with one code, one executable, and one work-  
715 flow (L. Harris, Zhou, Lin, et al., 2020). Those new options include:

- 716 • New cloud fraction diagnostic schemes;
- 717 • New cloud ice nucleation schemes;
- 718 • New cloud ice generation schemes;
- 719 • New cloud ice fall velocity diagnostic schemes;
- 720 • New cloud water and cloud ice effective radii diagnostic schemes;
- 721 • New radar reflectivity diagnostic schemes;
- 722 • Wegener-Bergeron-Findeisen process;
- 723 • New particle size distribution options;
- 724 • New cloud condensation nuclei calculation.

## 725 Data Availability Statement

726 The source codes of SHIELD are available at [https://doi.org/10.5281/zenodo](https://doi.org/10.5281/zenodo.5800223)  
727 [.5800223](https://doi.org/10.5281/zenodo.5800223). The corresponding data is available at [https://doi.org/10.5281/zenodo](https://doi.org/10.5281/zenodo.5800259)  
728 [.5800259](https://doi.org/10.5281/zenodo.5800259). The COSP2 software package can be accessed from [https://github.com/](https://github.com/CFMIP/COSPv2.0)  
729 [CFMIP/COSPv2.0](https://github.com/CFMIP/COSPv2.0).

730 The MERRA2 data can be obtained from [https://goldsmr5.gesdisc.eosdis.nasa](https://goldsmr5.gesdisc.eosdis.nasa.gov/data)  
731 [.gov/data](https://goldsmr5.gesdisc.eosdis.nasa.gov/data). The ERA5 data can be obtained from [https://cds.climate.copernicus](https://cds.climate.copernicus.eu/#!/search?text=ERA5&type=dataset)  
732 [.eu/#!/search?text=ERA5&type=dataset](https://cds.climate.copernicus.eu/#!/search?text=ERA5&type=dataset). The CALIPSO-GOCCP data can be ob-  
733 tained from [https://climserv.ipsl.polytechnique.fr/cfmip-obs/Calipso\\_goccp](https://climserv.ipsl.polytechnique.fr/cfmip-obs/Calipso_goccp.html)  
734 [.html](https://climserv.ipsl.polytechnique.fr/cfmip-obs/Calipso_goccp.html). The GPM data can be obtained from [https://disc.gsfc.nasa.gov/datasets/](https://disc.gsfc.nasa.gov/datasets/GPM_3IMERGHH_06/summary?keywords=gpm%20imerg)  
735 [GPM\\_3IMERGHH\\_06/summary?keywords=gpm%20imerg](https://disc.gsfc.nasa.gov/datasets/GPM_3IMERGHH_06/summary?keywords=gpm%20imerg).

## 736 Acknowledgments

737 The authors want to thank Dr. Shian-Jiann Lin, who developed the early version of the  
738 GFDL cloud microphysics scheme more than ten years ago. His great ideas and philoso-  
739 phy are still in the latest version of this scheme. Many thanks also go to the GFDL FV3  
740 team, who support the development of the GFDL MP in many ways. The authors also  
741 want to thank Dr. Songmiao Fan, Dr. Zhihong Tan, and Dr. Nadir Jeevanjee for their  
742 valuable comments and suggestions to improve the quality of this manuscript.

## 743 References

- 744 Arnold, N. P., Putman, W. M., & Freitas, S. R. (2020). Impact of resolution and  
745 parameterized convection on the diurnal cycle of precipitation in a global non-  
746 hydrostatic model [Journal Article]. *Journal of the Meteorological Society of*  
747 *Japan. Ser. II*, 98(6), 1279-1304. doi: 10.2151/jmsj.2020-066
- 748 Baldauf, M., Seifert, A., Forstner, J., Majewski, D., Raschendorfer, M., & Reinhardt,  
749 T. (2011). Operational convective-scale numerical weather prediction with the  
750 cosmo model: Description and sensitivities [Journal Article]. *Monthly Weather*  
751 *Review*, 139(12), 3887-3905. doi: 10.1175/MWR-D-10-05013.1
- 752 Bauer, P., Thorpe, A., & Brunet, G. (2015). The quiet revolution of numerical  
753 weather prediction [Journal Article]. *Nature*, 525(7567), 47-55. doi: 10.1038/  
754 nature14956
- 755 Beard, K. V., & Pruppacher, H. R. (1971). A wind tunnel investigation of the rate  
756 of evaporation of small water drops falling at terminal velocity in air [Jour-  
757 nal Article]. *Journal of the Atmospheric Sciences*, 28(8), 1455-1464. doi:  
758 10.1175/1520-0469(1971)028<1455:Awtiot>2.0.Co;2
- 759 Bigg, E. K. (1953). The supercooling of water [Journal Article]. *Proceedings of*  
760 *the Physical Society. Section B*, 66(8), 688-694. doi: 10.1088/0370-1301/66/8/

761  
762  
763  
764  
765  
766  
767  
768  
769  
770  
771  
772  
773  
774  
775  
776  
777  
778  
779  
780  
781  
782  
783  
784  
785  
786  
787  
788  
789  
790  
791  
792  
793  
794  
795  
796  
797  
798  
799  
800  
801  
802  
803  
804  
805  
806  
807  
808  
809  
810  
811  
812  
813  
814  
815

309

- Bodas-Salcedo, A., Webb, M. J., Bony, S., Chepfer, H., Dufresne, J. L., Klein, S. A., ... John, V. O. (2011). Cosp satellite simulation software for model assessment [Journal Article]. *Bulletin of the American Meteorological Society*, *92*(8), 1023-1043. doi: 10.1175/2011bams2856.1
- Boucher, O., & Lohmann, U. (1995). The sulfate-ccn-cloud albedo effect - a sensitivity study with 2 general-circulation models [Journal Article]. *Tellus Series B-Chemical and Physical Meteorology*, *47*(3), 281-300. doi: 10.1034/j.1600-0889.47.issue3.1.x
- Byers, H. R. (1965). *Elements of cloud physics* [Book]. Chicago: University of Chicago Press.
- Chen, J., Lin, S., Magnusson, L., Bender, M., Chen, X., Zhou, L., ... Harris, L. (2019). Advancements in hurricane prediction with noaa's next-generation forecast system [Journal Article]. *Geophysical Research Letters*, *46*(8), 4495-4501. doi: 10.1029/2019gl082410
- Chen, J. H., & Lin, S. J. (2011). The remarkable predictability of inter-annual variability of atlantic hurricanes during the past decade [Journal Article]. *Geophysical Research Letters*, *38*(11), n/a-n/a. doi: 10.1029/2011gl047629
- Chen, J. H., & Lin, S. J. (2013). Seasonal predictions of tropical cyclones using a 25-km-resolution general circulation model [Journal Article]. *Journal of Climate*, *26*(2), 380-398. doi: 10.1175/Jcli-D-12-00061.1
- Chen, J. H., Lin, S. J., Zhou, L. J., Chen, X., Rees, S., Bender, M., & Morin, M. (2019). Evaluation of tropical cyclone forecasts in the next generation global prediction system [Journal Article]. *Monthly Weather Review*, *147*(9), 3409-3428. doi: 10.1175/Mwr-D-18-0227.1
- Chepfer, H., Bony, S., Winker, D., Cesana, G., Dufresne, J. L., Minnis, P., ... Zeng, S. (2010). The gcm-oriented calipso cloud product (calipso-goccp) [Journal Article]. *Journal of Geophysical Research*, *115*(D4). doi: 10.1029/2009jd012251
- Dong, J., Liu, B., Zhang, Z., Wang, W., Mehra, A., Hazelton, A. T., ... Marks, F. (2020). The evaluation of real-time hurricane analysis and forecast system (hafs) stand-alone regional (sar) model performance for the 2019 atlantic hurricane season [Journal Article]. *Atmosphere*, *11*(6). doi: 10.3390/atmos11060617
- Ek, M. B., Mitchell, K. E., Lin, Y., Rogers, E., Grunmann, P., Koren, V., ... Tarp-ley, J. D. (2003). Implementation of noah land surface model advances in the national centers for environmental prediction operational mesoscale eta model [Journal Article]. *Journal of Geophysical Research-Atmospheres*, *108*(D22), n/a-n/a. doi: 10.1029/2002jd003296
- Fan, J. W., Wang, Y., Rosenfeld, D., & Liu, X. H. (2016). Review of aerosol-cloud interactions: Mechanisms, significance, and challenges [Journal Article]. *Journal of the Atmospheric Sciences*, *73*(11), 4221-4252. Retrieved from <GotoISI>://WOS:000386007800001 doi: 10.1175/Jas-D-16-0037.1
- Federer, B., & Waldvogel, A. (1975). Hail and raindrop size distributions from a swiss multicell storm [Journal Article]. *Journal of Applied Meteorology*, *14*(1), 91-97. doi: 10.1175/1520-0450(1975)014<0091:Harsdf>2.0.Co;2
- Forbes, R., & Tompkins, A. (2011). An improved representation of cloud and precipitation [Meteorology]. , 13-18. doi: 10.21957/nfgulzhe
- Forbes, R., Tompkins, A., & Untch, A. (2011, 09). A new prognostic bulk micro-physics scheme for the ifs. (649), 22. doi: 10.21957/bf6vjvxx
- Fu, Q. A. (1996). An accurate parameterization of the solar radiative properties of cirrus clouds for climate models [Journal Article]. *Journal of Climate*, *9*(9), 2058-2082. doi: 10.1175/1520-0442(1996)009<2058:Aapots>2.0.Co;2
- Gao, K., Chen, J. H., Harris, L. M., Lin, S. J., Xiang, B. Q., & Zhao, M. (2017). Impact of intraseasonal oscillations on the tropical cyclone activity over the gulf of mexico and western caribbean sea in gfdl hiram [Journal Article].

- 816 *Journal of Geophysical Research-Atmospheres*, 122(24), 13125-13137. doi:  
817 10.1002/2017jd027756
- 818 Gao, K., Harris, L., Chen, J. H., Lin, S. J., & Hazelton, A. (2019). Improv-  
819 ing agcm hurricane structure with two-way nesting [Journal Article].  
820 *Journal of Advances in Modeling Earth Systems*, 11(1), 278-292. doi:  
821 10.1029/2018ms001359
- 822 Gelaro, R., McCarty, W., Suarez, M. J., Todling, R., Molod, A., Takacs, L., ...  
823 Zhao, B. (2017). The modern-era retrospective analysis for research and ap-  
824 plications, version 2 (merra-2) [Journal Article]. *J Clim*, Volume 30(Iss 13),  
825 5419-5454. doi: 10.1175/JCLI-D-16-0758.1
- 826 Gunn, K. L. S., & Marshall, J. S. (1958). The distribution with size of aggregate  
827 snowflakes [Journal Article]. *Journal of Meteorology*, 15(5), 452-461. doi: 10  
828 .1175/1520-0469(1958)015<0452:Tdwsoa>2.0.Co;2
- 829 Guo, H., Ming, Y., Fan, S., Zhou, L., Harris, L., & Zhao, M. (2021). Two-moment  
830 bulk cloud microphysics with prognostic precipitation in gfdl's atmosphere  
831 model am4.0: Configuration and performance [Journal Article]. *Jour-  
832 nal of Advances in Modeling Earth Systems*, 13(6), e2020MS002453. doi:  
833 10.1029/2020ms002453
- 834 Han, J., & Bretherton, C. S. (2019). Tke-based moist eddy-diffusivity mass-  
835 flux (edmf) parameterization for vertical turbulent mixing [Journal Article].  
836 *Weather and Forecasting*, 34(4), 869-886. doi: 10.1175/Waf-D-18-0146.1
- 837 Han, J. G., Wang, W. G., Kwon, Y. C., Hong, S. Y., Tallapragada, V., & Yang,  
838 F. L. (2017). Updates in the ncep gfs cumulus convection schemes with scale  
839 and aerosol awareness [Journal Article]. *Weather and Forecasting*, 32(5),  
840 2005-2017. doi: 10.1175/Waf-D-17-0046.1
- 841 Harris, L., Chen, X., Zhou, L., & Chen, J.-H. (2020). The nonhydrostatic solver of  
842 the gfdl finite-volume cubed-sphere dynamical core [Journal Article].  
843 doi: <https://doi.org/10.25923/9wdt-4895>
- 844 Harris, L., Zhou, L., Chen, X., & Chen, J.-H. (2020). The gfdl finite-volume cubed-  
845 sphere dynamical core: Release 201912 [Journal Article].  
846 doi: <https://doi.org/10.25923/7h88-c534>
- 847 Harris, L., Zhou, L., Lin, S., Chen, J., Chen, X., Gao, K., ... Stern, W. (2020). Gfdl  
848 shield: A unified system for weather-to-seasonal prediction [Journal Article].  
849 *Journal of Advances in Modeling Earth Systems*, 12(10), e2020MS002223. doi:  
850 10.1029/2020ms002223
- 851 Harris, L. M., & Lin, S. J. (2013). A two-way nested global-regional dynamical core  
852 on the cubed-sphere grid [Journal Article]. *Monthly Weather Review*, 141(1),  
853 283-306. doi: 10.1175/Mwr-D-11-00201.1
- 854 Harris, L. M., Lin, S. J., & Tu, C. Y. (2016). High-resolution climate simulations  
855 using gfdl hiram with a stretched global grid [Journal Article]. *Journal of Cli-  
856 mate*, 29(11), 4293-4314. doi: 10.1175/Jcli-D-15-0389.1
- 857 Harris, L. M., Rees, S. L., Morin, M., Zhou, L., & Stern, W. F. (2019). Explicit pre-  
858 diction of continental convection in a skillful variable-resolution global model  
859 [Journal Article]. *Journal of Advances in Modeling Earth Systems*, 11(6),  
860 1847-1869. doi: 10.1029/2018ms001542
- 861 Hazelton, A., Alaka, G. J., Cowan, L., Fischer, M., & Gopalakrishnan, S. (2021).  
862 Understanding the processes causing the early intensification of hurricane do-  
863 rian through an ensemble of the hurricane analysis and forecast system (hafs)  
864 [Journal Article]. *Atmosphere*, 12(1). doi: 10.3390/atmos12010093
- 865 Hazelton, A. T., Harris, L., & Lin, S. J. (2018). Evaluation of tropical cyclone  
866 structure forecasts in a high-resolution version of the multiscale gfdl fvgfs  
867 model [Journal Article]. *Weather and Forecasting*, 33(2), 419-442. doi:  
868 10.1175/Waf-D-17-0140.1
- 869 He, B., Bao, Q., Wang, X. C., Zhou, L. J., Wu, X. F., Liu, Y. M., ... Zhang, X. Q.  
870 (2019). Cas fgoals-f3-l model datasets for cmip6 historical atmospheric model

- 871 intercomparison project simulation [Journal Article]. *Advances in Atmospheric*  
872 *Sciences*, 36(8), 771-778. doi: 10.1007/s00376-019-9027-8
- 873 Hersbach, H., Bell, B., Berrisford, P., Hirahara, S., Horanyi, A., Muñoz-Sabater, J.,  
874 ... Thepaut, J. N. (2020). The era5 global reanalysis [Journal Article]. *Quar-*  
875 *terly Journal of the Royal Meteorological Society*, 146(730), 1999-2049. doi:  
876 10.1002/qj.3803
- 877 Hoke, J. E., Phillips, N. A., Dimego, G. J., Tuccillo, J. J., & Sela, J. G. (1989).  
878 The regional analysis and forecast system of the national meteorological  
879 center [Journal Article]. *Weather and Forecasting*, 4(3), 323-334. doi:  
880 10.1175/1520-0434(1989)004<0323:Traafs>2.0.Co;2
- 881 Hong, Y., Hsu, K.-L., Sorooshian, S., & Gao, X. (2004). Precipitation estimation  
882 from remotely sensed imagery using an artificial neural network cloud clas-  
883 sification system [Journal Article]. *Journal of Applied Meteorology*, 43(12),  
884 1834-1853. doi: 10.1175/JAM2173.1
- 885 Houze, R. A. (2014). *Cloud dynamics* (Second edition. ed.) [Book]. Amsterdam ;  
886 New York: Academic Press is an imprint of Elsevier.
- 887 Houze, R. A., Hobbs, P. V., Herzegh, P. H., & Parsons, D. B. (1979). Size  
888 distributions of precipitation particles in frontal clouds [Journal Arti-  
889 cle]. *Journal of the Atmospheric Sciences*, 36(1), 156-162. doi: 10.1175/  
890 1520-0469(1979)036<0156:Sdoppi>2.0.Co;2
- 891 Huang, B., Wang, X., Kleist, D. T., & Lei, T. (2021). A simultaneous multiscale  
892 data assimilation using scale-dependent localization in gsi-based hybrid 4den-  
893 var for ncep fv3-based gfs [Journal Article]. *Monthly Weather Review*, 149(2),  
894 479-501. doi: 10.1175/mwr-d-20-0166.1
- 895 Ikawa, M., & Saito, K. (1991, 12). *Description of a nonhydrostatic model devel-*  
896 *oped at the forecast research department of the mri* (Technical Report No. 28).  
897 Meteorological Research Institute, Japan: Meteorological Research Institute,  
898 Japan. doi: 10.11483/mritechrepo.28
- 899 Jeevanjee, N. (2017). Vertical velocity in the gray zone [Journal Article].  
900 *Journal of Advances in Modeling Earth Systems*, 9(6), 2304-2316. doi:  
901 10.1002/2017ms001059
- 902 Khain, A. P., Beheng, K. D., Heymsfield, A., Korolev, A., Krichak, S. O., Levin,  
903 Z., ... Yano, J. I. (2015). Representation of microphysical processes in  
904 cloud-resolving models: Spectral (bin) microphysics versus bulk parame-  
905 terization [Journal Article]. *Reviews of Geophysics*, 53(2), 247-322. doi:  
906 10.1002/2014rg000468
- 907 Kogan, Y. (2013). A cumulus cloud microphysics parameterization for cloud-  
908 resolving models [Journal Article]. *Journal of the Atmospheric Sciences*, 70(5),  
909 1423-1436. doi: 10.1175/Jas-D-12-0183.1
- 910 Lamb, D., & Verlinde, J. (2011). *Physics and chemistry of clouds* [Book]. Cambridge  
911 ; New York: Cambridge University Press.
- 912 Leighton, H., Black, R., Zhang, X. J., Marks, F. D., & Gopalakrishnan, S. G. (2020).  
913 Ice particle size distributions from composites of microphysics observations col-  
914 lected in tropical cyclones [Journal Article]. *Geophysical Research Letters*,  
915 47(15), e2020GL088762. doi: 10.1029/2020GL088762
- 916 Li, J., Bao, Q., Liu, Y., Wu, G., Wang, L., He, B., ... Li, J. (2019). Evaluation  
917 of faml2 in simulating the climatology and seasonal-to-interannual variability  
918 of tropical cyclone characteristics [Journal Article]. *Journal of Advances in*  
919 *Modeling Earth Systems*, 11(4), 1117-1136. doi: 10.1029/2018ms001506
- 920 Lin, S.-J. (2004). A "vertically lagrangian" finite-volume dynamical core for global  
921 models [Journal Article]. *Monthly Weather Review*, 132(10), 2293-2307. doi:  
922 10.1175/1520-0493(2004)132<2293:Avlfdc>2.0.Co;2
- 923 Lin, Y. L., Farley, R. D., & Orville, H. D. (1983). Bulk parameterization of the snow  
924 field in a cloud model [Journal Article]. *Journal of Climate and Applied Meteo-*  
925 *rology*, 22(6), 1065-1092. doi: 10.1175/1520-0450(1983)022<1065:Bpotsf>2.0.Co;

926  
927  
928  
929  
930  
931  
932  
933  
934  
935  
936  
937  
938  
939  
940  
941  
942  
943  
944  
945  
946  
947  
948  
949  
950  
951  
952  
953  
954  
955  
956  
957  
958  
959  
960  
961  
962  
963  
964  
965  
966  
967  
968  
969  
970  
971  
972  
973  
974  
975  
976  
977  
978  
979  
980

- Liu, J. Y., & Orville, H. D. (1969). Numerical modeling of precipitation and cloud shadow effects on mountain-induced cumuli [Journal Article]. *Journal of the Atmospheric Sciences*, *26*(6), 1283-1298. doi: 10.1175/1520-0469(1969)026<1283:Nmopac>2.0.Co;2
- Marshall, J. S., & Palmer, W. M. (1948). The distribution of raindrops with size [Journal Article]. *Journal of Meteorology*, *5*(4), 165-166. doi: 10.1175/1520-0469(1948)005<0165:Tdorws>2.0.Co;2
- Martin, G. M., Johnson, D. W., & Spice, A. (1994). The measurement and parameterization of effective radius of droplets in warm stratocumulus clouds [Journal Article]. *Journal of the Atmospheric Sciences*, *51*(13), 1823-1842. doi: 10.1175/1520-0469(1994)051<1823:Tmapoe>2.0.Co;2
- Mason, B. J. (1971). *The physics of clouds* [Book]. Oxford: Clarendon Press.
- McFarquhar, G. M., Hsieh, T.-L., Freer, M., Mascio, J., & Jewett, B. F. (2015). The characterization of ice hydrometeor gamma size distributions as volumes in n0-lambda-mu phase space: Implications for microphysical process modeling [Journal Article]. *Journal of the Atmospheric Sciences*, *72*(2), 892-909. doi: 10.1175/jas-d-14-0011.1
- Milbrandt, J. A., & Yau, M. K. (2005). A multimoment bulk microphysics parameterization. part i: Analysis of the role of the spectral shape parameter [Journal Article]. *Journal of the Atmospheric Sciences*, *62*(9), 3051-3064. doi: 10.1175/Jas3534.1
- Morrison, H., & Gettelman, A. (2008). A new two-moment bulk stratiform cloud microphysics scheme in the community atmosphere model, version 3 (cam3). part i: Description and numerical tests [Journal Article]. *Journal of Climate*, *21*(15), 3642-3659. doi: 10.1175/2008jcli2105.1
- Morrison, H., & Grabowski, W. W. (2008). A novel approach for representing ice microphysics in models: Description and tests using a kinematic framework [Journal Article]. *Journal of the Atmospheric Sciences*, *65*(5), 1528-1548. doi: 10.1175/2007jas2491.1
- Morrison, H., & Milbrandt, J. A. (2015). Parameterization of cloud microphysics based on the prediction of bulk ice particle properties. part i: Scheme description and idealized tests [Journal Article]. *Journal of the Atmospheric Sciences*, *72*(1), 287-311. doi: 10.1175/Jas-D-14-0065.1
- Nogherotto, R., Tompkins, A. M., Giuliani, G., Coppola, E., & Giorgi, F. (2016). Numerical framework and performance of the new multiple-phase cloud microphysics scheme in regcm4.5: precipitation, cloud microphysics, and cloud radiative effects [Journal Article]. *Geoscientific Model Development*, *9*(7), 2533-2547. doi: 10.5194/gmd-9-2533-2016
- Patel, R. N., Yuter, S. E., Miller, M. A., Rhodes, S. R., Bain, L., & Peele, T. W. (2021). The diurnal cycle of winter season temperature errors in the operational global forecast system (gfs) [Journal Article]. *Geophysical Research Letters*, *48*(20), e2021GL095101. doi: 10.1029/2021gl095101
- Pollard, R. T., Rhines, P. B., & Thompson, R. O. R. Y. (1973). The deepening of the wind-mixed layer [Journal Article]. *Geophysical Fluid Dynamics*, *3*(4), 381-404. doi: 10.1080/03091927208236105
- Pruppacher, H. R., & Klett, J. D. (2010). *Microphysics of clouds and precipitation* (2nd ed.) [Book]. Springer Netherlands. doi: 10.1007/978-0-306-48100-0
- Putman, W. M., & Lin, S. H. (2007). Finite-volume transport on various cubed-sphere grids [Journal Article]. *Journal of Computational Physics*, *227*(1), 55-78. doi: 10.1016/j.jcp.2007.07.022
- Randles, C. A., Da Silva, A. M., Buchard, V., Colarco, P. R., Darmenov, A., Govindaraju, R., ... Flynn, C. J. (2017). The merra-2 aerosol reanalysis, 1980 - onward, part i: System description and data assimilation evaluation [Journal Article]. *J Clim*, *30*(17), 6823-6850. doi: 10.1175/JCLI-D-16-0609.1

- 981 Rasch, P. J., & Kristjánsson, J. E. (1998). A comparison of the ccm3 model climate  
982 using diagnosed and predicted condensate parameterizations [Journal Article].  
983 *Journal of Climate*, *11*(7), 1587-1614. doi: 10.1175/1520-0442(1998)011<1587:  
984 Acotcm>2.0.Co;2
- 985 Rienecker, M. M., Suarez, M. J., Gelaro, R., Todling, R., Bacmeister, J., Liu, E.,  
986 ... Woollen, J. (2011). Merra: Nasa's modern-era retrospective analysis  
987 for research and applications [Journal Article]. *Journal of Climate*, *24*(14),  
988 3624-3648. doi: 10.1175/Jcli-D-11-00015.1
- 989 Rotstayn, L. D. (1997). A physically based scheme for the treatment of stratiform  
990 clouds and precipitation in large-scale models. i: Description and evaluation of  
991 the microphysical processes [Journal Article]. *Quarterly Journal of the Royal  
992 Meteorological Society*, *123*(541), 1227-1282. doi: 10.1002/qj.49712354106
- 993 Seifert, A., & Beheng, K. D. (2005). A two-moment cloud microphysics pa-  
994 rameterization for mixed-phase clouds. part 1: Model description [Jour-  
995 nal Article]. *Meteorology and Atmospheric Physics*, *92*(1-2), 45-66. doi:  
996 10.1007/s00703-005-0112-4
- 997 Stephens, G. L., Li, J. L., Wild, M., Clayson, C. A., Loeb, N., Kato, S., ... An-  
998 drews, T. (2012). An update on earth's energy balance in light of the latest  
999 global observations [Journal Article]. *Nature Geoscience*, *5*(10), 691-696. doi:  
1000 10.1038/Ngeo1580
- 1001 Straka, J. M. (2009). *Cloud and precipitation microphysics* [Book]. Cambridge:  
1002 Cambridge University Press. doi: 10.1017/cbo9780511581168
- 1003 Swales, D. J., Pincus, R., & Bodas-Salcedo, A. (2018). The cloud feedback  
1004 model intercomparison project observational simulator package: Version  
1005 2 [Journal Article]. *Geoscientific Model Development*, *11*(1), 77-81. doi:  
1006 10.5194/gmd-11-77-2018
- 1007 Tiedtke, M. (1993). Representation of clouds in large-scale models [Journal Article].  
1008 *Monthly Weather Review*, *121*(11), 3040-3061. doi: 10.1175/1520-0493(1993)  
1009 121<3040:Rocils>2.0.Co;2
- 1010 Tong, M. J., Zhu, Y. Q., Zhou, L. J., Liu, E. M., Chen, M., Liu, Q. H., & Lin,  
1011 S. A. J. (2020). Multiple hydrometeors all-sky microwave radiance assimila-  
1012 tion in fv3gfs [Journal Article]. *Monthly Weather Review*, *148*(7), 2971-2995.  
1013 doi: 10.1175/Mwr-D-19-0231.1
- 1014 Trenberth, K. E., Fasullo, J. T., & Kiehl, J. (2009). Earth's global energy budget  
1015 [Journal Article]. *Bulletin of the American Meteorological Society*, *90*(3), 311-  
1016 323. doi: 10.1175/2008bams2634.1
- 1017 Tripoli, G. J., & Cotton, W. R. (1980). A numerical investigation of several factors  
1018 contributing to the observed variable intensity of deep convection over south  
1019 florida [Journal Article]. *Journal of Applied Meteorology*, *19*(9), 1037-1063.  
1020 doi: 10.1175/1520-0450(1980)019<1037:Aniosf>2.0.Co;2
- 1021 Wild, M., Hakuba, M. Z., Folini, D., Dorig-Ott, P., Schar, C., Kato, S., & Long,  
1022 C. N. (2019). The cloud-free global energy balance and inferred cloud radiative  
1023 effects: an assessment based on direct observations and climate models [Jour-  
1024 nal Article]. *Clim Dyn*, *52*(7), 4787-4812. doi: 10.1007/s00382-018-4413-y
- 1025 Wisner, C., Myers, C., & Orville, H. D. (1972). Numerical model of a hail-bearing  
1026 cloud [Journal Article]. *Journal of the Atmospheric Sciences*, *29*(6), 1160-1181.  
1027 doi: 10.1175/1520-0469(1972)029<1160:Anmoah>2.0.Co;2
- 1028 Xu, K. M., & Randall, D. A. (1996). A semiempirical cloudiness parameteri-  
1029 zation for use in climate models [Journal Article]. *Journal of the Atmo-  
1030 spheric Sciences*, *53*(21), 3084-3102. doi: 10.1175/1520-0469(1996)053<3084:  
1031 Ascpfu>2.0.Co;2
- 1032 Zhao, Q. Y., Black, T. L., & Baldwin, M. E. (1997). Implementation of the  
1033 cloud prediction scheme in the eta model at ncep [Journal Article]. *Weather  
1034 and Forecasting*, *12*(3), 697-712. doi: 10.1175/1520-0434(1997)012<0697:  
1035 lotcps>2.0.Co;2

- 1036 Zhao, Q. Y., & Carr, F. H. (1997). A prognostic cloud scheme for operational nwp  
1037 models [Journal Article]. *Monthly Weather Review*, 125(8), 1931-1953. doi: 10  
1038 .1175/1520-0493(1997)125(1931:Apcsfo)2.0.Co;2
- 1039 Zhou, L. J., Bao, Q., Liu, Y. M., Wu, G. X., Wang, W. C., Wang, X. C., . . . Li,  
1040 J. D. (2015). Global energy and water balance: Characteristics from  
1041 finite-volume atmospheric model of the iap/lasg (famil1) [Journal Arti-  
1042 cle]. *Journal of Advances in Modeling Earth Systems*, 7(1), 1-20. doi:  
1043 10.1002/2014ms000349
- 1044 Zhou, L. J., Lin, S. J., Chen, J. H., Harris, L. M., Chen, X., & Rees, S. L. (2019).  
1045 Toward convective-scale prediction within the next generation global prediction  
1046 system [Journal Article]. *Bulletin of the American Meteorological Society*,  
1047 100(7), 1225-1243. doi: 10.1175/Bams-D-17-0246.1